

REPORT DOCUMENTATION PAGE			Form Approved OMB NO. 0704-0188		
<p>The public reporting burden for this collection of information is estimated to average 1 hour per response, including the time for reviewing instructions, searching existing data sources, gathering and maintaining the data needed, and completing and reviewing the collection of information. Send comments regarding this burden estimate or any other aspect of this collection of information, including suggestions for reducing this burden, to Washington Headquarters Services, Directorate for Information Operations and Reports, 1215 Jefferson Davis Highway, Suite 1204, Arlington VA, 22202-4302. Respondents should be aware that notwithstanding any other provision of law, no person shall be subject to any penalty for failing to comply with a collection of information if it does not display a currently valid OMB control number.</p> <p>PLEASE DO NOT RETURN YOUR FORM TO THE ABOVE ADDRESS.</p>					
1. REPORT DATE (DD-MM-YYYY) 07-07-2008		2. REPORT TYPE Final Report		3. DATES COVERED (From - To) 15-Apr-2005 - 14-Apr-2008	
4. TITLE AND SUBTITLE NAVIGATION AND HAZARD AVOIDANCE FOR HIGH-SPEED UNMANNED GROUND VEHICLES IN ROUGH TERRAIN			5a. CONTRACT NUMBER W911NF-05-1-0166		
			5b. GRANT NUMBER		
			5c. PROGRAM ELEMENT NUMBER 611102		
6. AUTHORS Karl Iagnemma			5d. PROJECT NUMBER		
			5e. TASK NUMBER		
			5f. WORK UNIT NUMBER		
7. PERFORMING ORGANIZATION NAMES AND ADDRESSES Massachusetts Institute of Technology Office of Sponsored Programs Bldg. E19-750 Cambridge, MA 02139 -4307			8. PERFORMING ORGANIZATION REPORT NUMBER		
9. SPONSORING/MONITORING AGENCY NAME(S) AND ADDRESS(ES) U.S. Army Research Office P.O. Box 12211 Research Triangle Park, NC 27709-2211			10. SPONSOR/MONITOR'S ACRONYM(S) ARO		
			11. SPONSOR/MONITOR'S REPORT NUMBER(S) 43531-CI.1		
12. DISTRIBUTION AVAILABILITY STATEMENT Approved for Public Release; Distribution Unlimited					
13. SUPPLEMENTARY NOTES The views, opinions and/or findings contained in this report are those of the author(s) and should not be construed as an official Department of the Army position, policy or decision, unless so designated by other documentation.					
14. ABSTRACT Many applications require unmanned ground vehicles (UGVs) to travel at high speeds on sloped, natural terrain. Control of UGVs in these scenarios is difficult due to the inherent complexity in modeling terrain effects on vehicle motion. This research has studied methods for control of high speed UGVs through the use of simplified models of UGV dynamics and terrain interaction. Simulation and experimental results gathered during this work has demonstrated the effectiveness of two distinct control approaches. Other work conducted under this grant has focused on modeling of omnidirectional vehicles. Future work will pursue control methods for high speed, omnidirectional UGVs in rough, uneven terrain.					
15. SUBJECT TERMS Robotics, unmanned ground vehicles, control, terrain					
16. SECURITY CLASSIFICATION OF:			17. LIMITATION OF ABSTRACT SAR	15. NUMBER OF PAGES	19a. NAME OF RESPONSIBLE PERSON Steven Dubowsky
a. REPORT U	b. ABSTRACT U	c. THIS PAGE U			19b. TELEPHONE NUMBER 617-253-2144

Report Title

NAVIGATION AND HAZARD AVOIDANCE FOR HIGH-SPEED UNMANNED GROUND VEHICLES IN ROUGH TERRAIN

ABSTRACT

Many applications require unmanned ground vehicles (UGVs) to travel at high speeds on sloped, natural terrain. Control of UGVs in these scenarios is difficult due to the inherent complexity in modeling terrain effects on vehicle motion. This research has studied methods for control of high speed UGVs through the use of simplified models of UGV dynamics and terrain interaction. Simulation and experimental results gathered during this work has demonstrated the effectiveness of two distinct control approaches. Other work conducted under this grant has focused on modeling of omnidirectional vehicles. Future work will pursue control methods for high speed, omnidirectional UGVs in rough, uneven terrain.

List of papers submitted or published that acknowledge ARO support during this reporting period. List the papers, including journal references, in the following categories:

(a) Papers published in peer-reviewed journals (N/A for none)

Spenko, M., Kuroda, Y., Dubowsky, S., and Iagnemma, K., "Hazard Avoidance for High Speed Unmanned Ground Vehicles in Rough Terrain," Journal of Field Robotics, Volume 23, No. 5, pp. 311-331, May, 2006

Shimoda, S., Kuroda, Y., Iagnemma, K., "Potential Field Navigation of High Speed Vehicles on Rough Terrain," Robotica, Vol. 25, No. 4, pp 409-424, July 2007

Udengaard, M., and Iagnemma, K., "Analysis, Design, and Control of an Omnidirectional Mobile Robot in Rough Terrain," submitted to the IEEE/ASME Transactions on Mechatronics, 2008

Number of Papers published in peer-reviewed journals: 3.00

(b) Papers published in non-peer-reviewed journals or in conference proceedings (N/A for none)

Number of Papers published in non peer-reviewed journals: 0.00

(c) Presentations

Number of Presentations: 0.00

Non Peer-Reviewed Conference Proceeding publications (other than abstracts):

Number of Non Peer-Reviewed Conference Proceeding publications (other than abstracts): 0

Peer-Reviewed Conference Proceeding publications (other than abstracts):

Spenko, M., Overholt, J., and Iagnemma, K., “High Speed Hazard Avoidance for Unmanned Ground Vehicles in Emergency Situations,” Proceedings of the 25th Army Science Conference, 2006

Spenko, M., Dubowsky, S., and Iagnemma, K., “Experimental Validation of High Speed Hazard Avoidance Control for Unmanned Ground Vehicles,” Proceedings of the 8th International IFAC Symposium on Robot Control, SYROCO, 2006

Udengaard, M., and Iagnemma, K., “Kinematic Analysis and Control of an Omnidirectional Mobile Robot in Rough Terrain,” Proceedings of the IEEE/RSJ International Conference on Intelligent Robots and Systems, 2007

Udengaard, M., and Iagnemma, K., “Design of an Omnidirectional Mobile Robot for Rough Terrain,” proceedings of the IEEE International Conference on Robotics and Automation 2008

Iagnemma, K., Shimoda, S., and Shiller, Z., “Near-Optimal Navigation of High Speed Mobile Robots on Uneven Terrain,” to appear in the Proceedings of the International Conference on Intelligent Robots and Systems, 2008

Udengaard, M., and Iagnemma, K., "Design of a Highly Maneuverable Wheeled Mobile Robot," proceedings of the SPIE Conference on Unmanned Systems, 2008

Number of Peer-Reviewed Conference Proceeding publications (other than abstracts): 6

(d) Manuscripts

Number of Manuscripts: 0.00

Number of Inventions:

Graduate Students

<u>NAME</u>	<u>PERCENT SUPPORTED</u>
Martin Udengaard	1.00
FTE Equivalent:	1.00
Total Number:	1

Names of Post Doctorates

<u>NAME</u>	<u>PERCENT SUPPORTED</u>
FTE Equivalent:	
Total Number:	

Names of Faculty Supported

<u>NAME</u>	<u>PERCENT SUPPORTED</u>	National Academy Member
Steven Dubowsky	0.05	No
Karl Iagnemma	0.25	No
FTE Equivalent:	0.30	
Total Number:	2	

Names of Under Graduate students supported

<u>NAME</u>	<u>PERCENT SUPPORTED</u>
FTE Equivalent:	
Total Number:	

Student Metrics

This section only applies to graduating undergraduates supported by this agreement in this reporting period

The number of undergraduates funded by this agreement who graduated during this period: 0.00

The number of undergraduates funded by this agreement who graduated during this period with a degree in science, mathematics, engineering, or technology fields:..... 0.00

The number of undergraduates funded by your agreement who graduated during this period and will continue to pursue a graduate or Ph.D. degree in science, mathematics, engineering, or technology fields:..... 0.00

Number of graduating undergraduates who achieved a 3.5 GPA to 4.0 (4.0 max scale): 0.00

Number of graduating undergraduates funded by a DoD funded Center of Excellence grant for Education, Research and Engineering:..... 0.00

The number of undergraduates funded by your agreement who graduated during this period and intend to work for the Department of Defense 0.00

The number of undergraduates funded by your agreement who graduated during this period and will receive scholarships or fellowships for further studies in science, mathematics, engineering or technology fields: 0.00

Names of Personnel receiving masters degrees

NAME

Martin Udengaard

Total Number:

1

Names of personnel receiving PhDs

NAME

Total Number:

Names of other research staff

NAME

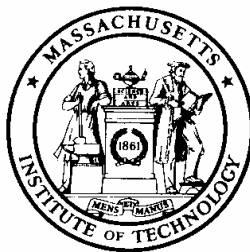
PERCENT SUPPORTED

FTE Equivalent:

Total Number:

Sub Contractors (DD882)

Inventions (DD882)



**NAVIGATION AND HAZARD AVOIDANCE FOR HIGH-SPEED
UNMANNED GROUND VEHICLES IN ROUGH TERRAIN**

ARO Award Number: W911NF-05-1-0166

Final Report
April 15, 2005 – April 14, 2008

Prepared for:

U.S. Army Research Office
Systems and Control Division
P.O. Box 12211
4300 South Miami Blvd.
Research Triangle Park, NC 27709-2211

Attention:
Dr. Randy Zachery
Tel: (919) 549-4368, Fax: (919) 549-4354
Email: randy.zachery@us.army.mil

Technical POC:
Dr. Karl Iagnemma
Department of Mechanical Engineering
Massachusetts Institute of Technology
77 Massachusetts Avenue, Room 3-435a
Cambridge, MA 02139
Tel #: 617-452-3262 Fax #: 617-253-9637
Email: kdi@mit.edu

Foreword

Many applications require unmanned ground vehicles (UGVs) to travel at high speeds on sloped, natural terrain. Control of UGVs in these scenarios is difficult due to the inherent complexity in modeling terrain effects on vehicle motion. This research has studied methods for control of high speed UGVs through the use of simplified models of UGV dynamics and terrain interaction. Simulation and experimental results gathered during this work has demonstrated the effectiveness of two distinct control approaches. Other work conducted under this grant has focused on modeling of omnidirectional vehicles. Future work will pursue control methods for high speed, omnidirectional UGVs in rough, uneven terrain.

Keywords: Mobile robots, potential fields, outdoor terrain, motion planning

Table of Contents

FOREWARD	1
TABLE OF CONTENTS.....	2
PROBLEM STATEMENT	3
SUMMARY OF RESULTS	4
APPENDIX A: High Speed Navigation of Unmanned Ground Vehicles on Uneven Terrain Using Potential Fields	6
APPENDIX B: Near-Optimal Navigation of High Speed Mobile Robots on Uneven Terrain	52
APPENDIX C: Analysis, Design, and Control of an Omnidirectional Mobile Robot in Rough Terrain	58

Problem Statement

Unmanned ground vehicles (UGVs) have important military, reconnaissance, and materials handling applications, and are expected to play a significant role in future Army operations as part of the Future Combat Systems (FCS) program. Many applications require a UGV to move at high speeds through rugged, natural terrain of varying composition. For example, a UGV on a reconnaissance mission might be required to autonomously navigate at high speed along a pre-defined perimeter, through sandy, rocky, sloped, and vegetation-covered terrain. Increased speed over terrain can reduce detection risk, increase overall convoy speed, and generally increase UGV effectiveness.

High speed autonomous navigation in rough terrain is challenging for many reasons. Sources of difficulty include nonlinear UGV dynamic effects such as wheel slip, skid, ballistic behavior, roll over, and vehicle-terrain interaction. These factors can strongly influence system performance, particularly on loose, steeply sloped, or very rough terrain. Another difficulty is that UGV sensors can contain significant error and uncertainty. High speed operation also requires that navigation algorithms run in real time, and thus there is little time for complex computation. Finally, even with accurate models and precise sensing, unexpected situations are likely to occur that will require UGVs to perform emergency hazard avoidance maneuvers. (For example, a UGV moving at high speed might not detect a ditch or shell crater until it is close by, due to fundamental limitations of on-board range sensors.)

Model-based approaches to navigation and hazard avoidance are attractive since they can yield insight into UGV dynamics on varying terrain conditions. This is in contrast to approaches that rely on ad hoc rules to adapt UGV performance to changing conditions. However, at high speeds there is little time to perform model-based navigation methods that employ detailed vehicle and terrain models. Furthermore, it is difficult to accurately model complex tire/terrain interactions due to uncertainty about terrain conditions. Therefore, despite the attractiveness of model-based navigation algorithms, they are difficult to apply in real time.

The purpose of this three-year research program has been to investigate novel algorithms for high speed autonomous navigation and hazard avoidance based on the concept of the trajectory space, which is a compact framework for describing a UGV's dynamic performance on uneven, natural terrain. The trajectory space defines the performance limits of a UGV as a function of vehicle parameters, estimated terrain parameters (including inclination, roughness, and vehicle-terrain interaction), and hazard properties. Complex dynamic analysis is performed offline, and the results are stored in a look-up table as constraints in the trajectory space, allowing for extremely fast ($O(\mu s)$) on-line computation times. The trajectory space can also robustly consider uncertainty present in vehicle and terrain models and parameter estimates.

Other work conducted under this grant has focused on modeling of omnidirectional vehicles. Omnidirectional vehicles are those that are able to (kinematically) move in any direction instantaneously, regardless of pose. Such vehicles are of significant interest due to their extremely high agility, and ability to move in constricted, cluttered environments.

Summary of Results

The work conducted under this grant has fallen into three primary areas. These areas, and the major result(s) for each area, are described here.

- **Area 1:** The study of a class of high speed UGV control algorithms based on the “trajectory space,” a compact framework for describing a UGV’s dynamic performance on uneven, natural terrain.
 - **Major result:** Simulation and experimental results show that the control method can successfully navigate a small UGV between pre-defined waypoints at speeds up to 7.0 m/s, while avoiding static hazards, even while operating on significant side-slopes and in outdoor terrain.
 - **Major result:** A method were developed for utilizing simple, computationally efficient models of UGV motion on sloped terrain to avoid vehicle rollover and skidding. A method was proposed for explicitly considering the effect of terrain roughness (i.e. fine-grained height variation) on path following accuracy.
 - **Minor result:** The concept of the potential field, which has been widely employed in the robotics community, was here successfully extended to a novel class of systems.
 - **Note that the primary publication resulting from this work is contained in Appendix A.** It thoroughly describes the research results that are the product of this area of investigation. Other relevant publications include:
 - i. Spenko, M., Kuroda, Y., Dubowsky, S., and Iagnemma, K., “Hazard Avoidance for High Speed Unmanned Ground Vehicles in Rough Terrain,” *Journal of Field Robotics*, Volume 23, No. 5, pp. 311-331, May, 2006
 - ii. Spenko, M., Overholt, J., and Iagnemma, K., “High Speed Hazard Avoidance for Unmanned Ground Vehicles in Emergency Situations,” *Proceedings of the 25th Army Science Conference*, 2006
 - iii. Spenko, M., Dubowsky, S., and Iagnemma, K., “Experimental Validation of High Speed Hazard Avoidance Control for Unmanned Ground Vehicles,” *Proceedings of the 8th International IFAC Symposium on Robot Control, SYROCO*, 2006
- **Area 2:** The study of a high speed UGV control algorithm that fuses elements of the “trajectory space” method with a method based on optimal control to result in a method for near-optimal navigation of high speed mobile robots on uneven terrain.

- **Major result:** Simulation results show that the control method can successfully navigate a UGV across uneven terrain in a manner that lies (on average) within 10% of the time-optimal solution, however at a fraction of the computational cost.
 - **Minor result:** It was shown that a control method based on the principle of the trajectory space could be utilized as a “low level” controller in a layered control architecture, with excellent results.
 - **Note that the primary publication resulting from this work is contained in Appendix B.** It thoroughly describes the research results that are the product of this area of investigation.
-
- **Area 3:** The study of kinematic models of omnidirectional vehicles (i.e. vehicles that are able to (kinematically) move in any direction instantaneously, regardless of pose. Specifically, the kinematics of such vehicles were studied for the case of rough terrain operation.
 - **Major result:** A complete description of the kinematics of a class of omnidirectional vehicles driven by Active Split Offset Casters (ASOC) modules operating on uneven terrain.
 - **Major result:** A quantitative analysis of the effect of ASOC module kinematic parameter variation, terrain inclination, and terrain roughness on vehicle mobility was performed, and design guidelines were developed based on these results.
 - **Minor result:** Based on the analysis performed in this work, the design of an omnidirectional mobile robot intended for operation in rough terrain was developed. This design is currently under development with support from other Army research funds
 - **Note that the primary publication resulting from this work is contained in Appendix C.** It thoroughly describes the research results that are the product of this area of investigation. Other relevant publications include:
 - i. Udengaard, M., and Iagnemma, K., “Kinematic Analysis and Control of an Omnidirectional Mobile Robot in Rough Terrain,” *Proceedings of the IEEE/RSJ International Conference on Intelligent Robots and Systems*, 2007
 - ii. Udengaard, M., and Iagnemma, K., “Design of an Omnidirectional Mobile Robot for Rough Terrain,” *Proceedings of the IEEE International Conference on Robotics and Automation*, 2008
 - iii. Udengaard, M., and Iagnemma, K., "Design of a Highly Maneuverable Wheeled Mobile Robot," *Proceedings of the SPIE Conference on Unmanned Systems*, 2008

High Speed Navigation of Unmanned Ground Vehicles on Uneven Terrain Using Potential Fields

Shingo Shimoda^{*1,*2}, Yoji Kuroda^{*1} and Karl Iagnemma^{*1}

^{*1} : Massachusetts Institute of Technology
Department of Mechanical Engineering
Cambridge, MA 02139 USA

^{*2} : RIKEN, Biomimetic Control Research Center

Abstract

Many applications require unmanned ground vehicles (UGVs) to travel at high speeds on sloped, natural terrain. In this paper a potential field-based method is proposed for UGV navigation in such scenarios. In the proposed approach, a potential field is generated in the two-dimensional “trajectory space” of the UGV path curvature and longitudinal velocity. In contrast to traditional potential field methods, dynamic constraints and the effect of changing terrain conditions can be easily expressed in the proposed framework. A maneuver is chosen within a set of performance bounds, based on the local potential field gradient. It is shown that the proposed method is subject to local maxima problems, rather than local minima. A simple randomization technique is proposed to address this problem. Simulation and experimental results show that the proposed method can successfully navigate a small UGV between pre-defined waypoints at speeds up to 7.0 m/s, while avoiding static hazards. Further, vehicle curvature and velocity are controlled during vehicle motion to avoid rollover and excessive side slip. The method is computationally efficient, and thus suitable for on-board real-time implementation

Keywords: Mobile robots, potential fields, outdoor terrain, motion planning

1. Introduction and Related Work

Unmanned ground vehicles (UGVs) are expected to play significant roles in future military, planetary exploration, and materials handling applications [1,2]. Many applications require UGVs to move at high speeds over rough, natural terrain. One important challenge for high speed navigation lies in avoiding dynamically inadmissible maneuvers (i.e. maneuvers that self-induce vehicle failure due to rollover and excessive side slip)[3]. This is challenging as it requires real-time analysis of vehicle dynamics, and consideration of the effects of terrain inclination, roughness, and traction. Another challenge for high speed navigation lies in rapidly avoiding static hazards such as trees, large rocks or boulders, water traps, etc[4]. Such hazards are often detected at short range (particularly “negative obstacles,” or depressions below the nominal ground plane), and thus hazard avoidance maneuvers must be generated very rapidly.

Artificial potential fields have long been successfully employed for robot control and motion planning due to their effectiveness and computational efficiency. Generally, these methods construct artificial potential functions in a robot’s workspace such that the function’s global minimum value lies at the robot’s goal position and local maxima lie at locations of obstacles. The robot is “pushed” by an artificial force proportional to the potential function gradient at the robot’s position, and thus moves toward the goal position while avoiding hazards.

First works based on this approach were performed by Khatib as a real-time obstacle avoidance method for manipulators [5]. Latombe applied potential field methods to the general robot path planning problem, including high d.o.f. manipulators and mobile robots operating at low speeds in structured, planar environments [6]. This

work proposed various techniques for implementing potential field-based planning methods that do not suffer from local minima, a classical problem for potential field planners. Ge et al. applied the potential field concept for dynamic control of a mobile robot, with moving obstacles and goal in a structured environment [7]. This work addressed the local minima problem by judiciously choosing appropriate forms of the potential functions. Decision-making logic was also integrated into the motion planning strategy to avoid local minima. Path planning using potential fields has also been applied to parallel computation schemes and nonholonomic systems [8,9]. In summary, potential fields have been applied extensively to the problem of path planning of manipulators and mobile robots operating at low speeds in structured, indoor settings [10-14]. These methods do not consider the effects of terrain inclination, roughness, and traction on UGV mobility, nor do they address the problem of dynamically inadmissible maneuvers.

The application of artificial potential fields to mobile robot navigation in natural terrain has recently been addressed [15]. This approach relies on a vision-based classification algorithm to analyze local terrain and determine the locations of obstacles and nontraversable terrain regions. A conventional potential field planner is then applied to the 2-D traversability map. Since the approach is designed for low-speed operation on relatively flat, lightly cluttered environments it does not consider the effects of terrain inclination, roughness, or traction, nor does it address the problem of dynamically inadmissible maneuvers.

Here a local reactive navigation method is presented for high speed UGVs on rough, uneven terrain. In the proposed method, a potential field is defined in the two-dimensional “trajectory space” of the robot’s path curvature and longitudinal velocity

[19,20]. This is in contrast to other proposed methods, where potential fields are defined in the Cartesian or configuration space. The trajectory space framework allows dynamic constraints, terrain conditions, and navigation conditions (such as waypoint location(s), goal location, hazard location(s) and desired velocity) to be easily expressed as potential functions. A maneuver is chosen within a set of performance bounds, based on the potential field gradient. This yields a desired value for the UGV path curvature and velocity. Desired values for the UGVs steering angle and throttle can then be computed as inputs to low-level tracking controllers.

The proposed approach has some similarity to the dynamic window approach to navigation [16-18]. In that approach, a potential-like field is developed in the 2-dimensional space of translation and rotational velocities, and a behavior is chosen in the space. The method considers goal and obstacle locations, but does not consider dynamic constraints (due to rollover and side slip) and terrain conditions (such as inclination, roughness, and traction).

In Section 2 of this paper the trajectory space is introduced and problem assumptions are stated. In Section 3 potential functions are defined based on dynamic constraints, terrain conditions, and navigation conditions. In Section 4 the navigation algorithm is outlined. In Section 5 the problems of local minima and maxima are described, and a simple randomization technique for mitigating the effects of these problems is described. In Sections 6 and 7 simulation and experimental results are presented that show that the proposed method can successfully navigate a small UGV between pre-defined waypoints at speeds up to 7.0 m/s, while avoiding static hazards,

vehicle rollover and excessive side slip. The method is computationally efficient, and thus suitable for on-board real-time implementation.

2. Trajectory Space Description and Problem Assumptions

2.1 Trajectory Space Description

The trajectory space, $TS \in \mathbb{R}^2$, is defined as a two-dimensional space of a UGV's instantaneous path curvature and longitudinal velocity [19,20]. This space clearly cannot describe the complete vehicle state, but can rather capture important UGV state and configuration information and serve as a physically intuitive description of the current vehicle status. A UGV's "position" in TS is a curvature-velocity pair and is denoted $\tau = (\kappa, v)$. The relationship of a point in the trajectory space and a vehicle maneuver is shown in Figs. 1 (a) and (b). Note that in this work only positive longitudinal velocities are considered.

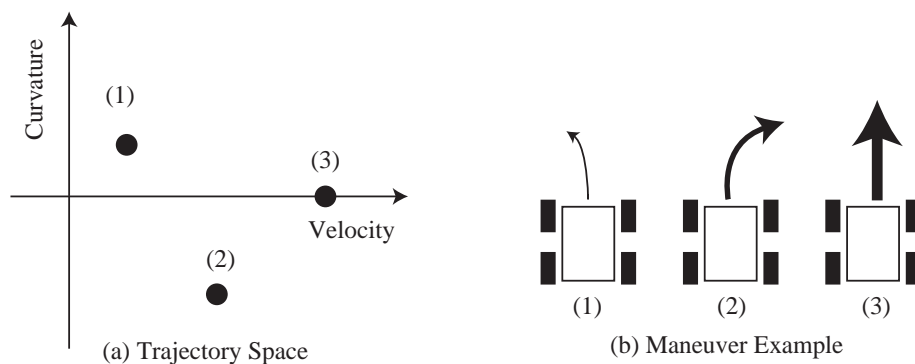


Fig. 1. Trajectory space illustration and maneuver examples corresponding to various locations in the trajectory space.

The trajectory space is a useful space for UGV navigation for two reasons. First, points in the trajectory space map easily and uniquely to the points in UGV actuation space (generally consisting of one throttle control input and one steering angle control

input). Thus navigation algorithms developed for use in the trajectory space will map to command inputs that obey vehicle nonholonomic constraints. Second, constraints related to dynamic effects such as UGV rollover and side slip are easily expressible in the trajectory space, since these effects are strong functions of the UGV velocity and path curvature [20]. Trajectory space constraints can also be formulated as functions of important terrain parameters, including terrain inclination, roughness, and traction.

In the proposed navigation method, a potential field is constructed in the trajectory space based on dynamic constraints, terrain conditions, and navigation conditions. An appropriate navigation command is then selected based on the properties of this field. Potential field formulation and a navigation methodology are discussed in Section 3.

2.2 Problem Assumptions

In this work it is assumed that the UGV has *a priori* knowledge of the positions of widely-spaced (i.e. many vehicle lengths) waypoint and/or goal locations[3,21,31]. Such knowledge is often derived from high-level path planning methods that rely on coarse elevation or topographical map data. It is assumed that the locations of hazards can be locally detected from on-board range sensors, and might take the form of terrain discontinuities such as rocks or ditches, or non-geometric hazards such as soft soil. Hazard detection and sensing issues are important aspects of UGV navigation in natural terrain, but are not a focus of this work.

It is also assumed that estimates of local terrain inclination, roughness, and traction can be sensed or estimated. The inclination of a UGV-sized terrain patch is defined in a body-fixed frame \mathbf{B} (see Fig. 2) by two parameters, θ and ϕ , associated with

the roll and pitch, respectively, of a plane fit to the patch. Roughness is defined as terrain unevenness caused by features that are less than one-half the vehicle wheel radius in size. Roughness is here characterized by the fractal dimension ϖ and is defined over the interval $\varpi \in [2,3]$ [22]. The maximum available traction at a wheel-terrain contact point is defined as the product of the terrain friction coefficient μ and the normal force acting on the terrain. This model assumes point contact between the wheel and terrain and neglects nonlinear effects due to wheel slip and terrain and/or tire deformation. Note that estimates of terrain inclination, roughness and traction can be derived from elevation and visual data via a variety of classification algorithms [22-25].

The vehicle mass, inertia tensor, center of gravity (c.g.) position, and kinematic properties are assumed to be known with reasonable certainty. The vehicle is assumed to be equipped with inertial and GPS sensors that allow measurement of the vehicle's linear rates and accelerations and position in space with reasonable certainty.

Coordinate systems employed in this work are shown in Fig. 2. A body frame \mathbf{B} is fixed to the vehicle, with its origin at the vehicle center of mass. The position of the vehicle in the inertial frame \mathbf{I} is expressed as the position of the origin of \mathbf{B} . The vehicle attitude is expressed by x - y - z Euler angles using the vehicle yaw ψ , roll θ , and pitch ϕ defined in \mathbf{B} . (Note that since the UGV suspension is assumed to be rigid the vehicle roll and pitch are equal to the terrain roll and pitch.) The vehicle wheelbase length is denoted L , the c.g. height from the ground is h , and the half-width is d . For simplicity the UGV is here assumed to be axially symmetric.

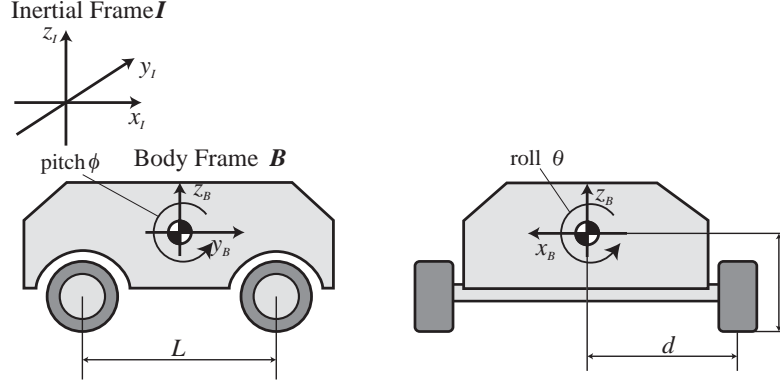


Fig. 2. Definition of UGV coordinate system.

3. Potential Field Definition

In the proposed method, a potential field is constructed in the trajectory space and vehicle maneuvers are selected based on the properties of this field. The potential field is defined as a sum of potential functions relating to each constraint, hazard, and goal or waypoint location. Here potential functions are defined for dynamic rollover and side slip constraints, waypoints (and goal) locations, hazard locations, and the desired UGV velocity.

3.1 Potential Functions for Rollover and Side Slip Constraints

During high speed operation a UGV must avoid dynamically inadmissible maneuvers, i.e. maneuvers that self-induce vehicle failure due to rollover and excessive side slip. This is challenging as it requires real-time analysis of vehicle dynamics, and consideration of the effects of terrain inclination, roughness, and traction. Note that although some side slip is expected and unavoidable, substantial slip that causes large heading or path following errors is detrimental. Roll-over is also generally undesirable despite the fact that some UGVs are designed to be mechanically invertible.

In the proposed approach, constraint functions related to rollover and side slip are computed from low-order dynamic models and expressed as potential function sources in the trajectory space. Clearly, higher d.o.f. models are available for predicting rollover and side slip, however the proposed models have been shown to be reasonably accurate in practice [17].

A rollover constraint for a UGV traveling on uneven terrain can be modeled as:

$$\kappa_r(v) = \frac{dg_z \pm hg_x}{hv^2} - \delta_r \quad (1)$$

where κ_r is the maximum admissible path curvature, v is the UGV longitudinal velocity, g_* is the gravitational acceleration of the $*$ -axis direction in \mathbf{B} . The two solutions to (1) correspond to travel on positive/negative inclination slopes, with nonzero g_x components reflecting the effect of terrain roll. Note that δ_r is introduced here as a small positive “safety margin” for reasons described below. A potential function is then defined as:

$$PF_r(\kappa, v) = \begin{cases} K_r \left(1 - \frac{(\kappa - \kappa_{MAX})^2}{(\kappa_r(v) - \kappa_{MAX})^2} \right) & \kappa_r < \kappa < \kappa_{MAX} \\ 0 & 0 \leq \kappa < \kappa_r \end{cases} \quad (2)$$

where κ_{MAX} is the maximum attainable path curvature for a UGV based on kinematic steering constraints, and is assumed to be independent of velocity. Here, K_r is a positive gain parameter to modulate the potential function height. The introduction of δ_r in equation (1) causes equation (2) to be non-zero at curvature-velocity pairs that approach but do not exceed the UGVs predicted stability limit. An illustration of a potential function for the UGV rollover constraint is shown in Fig. 3.

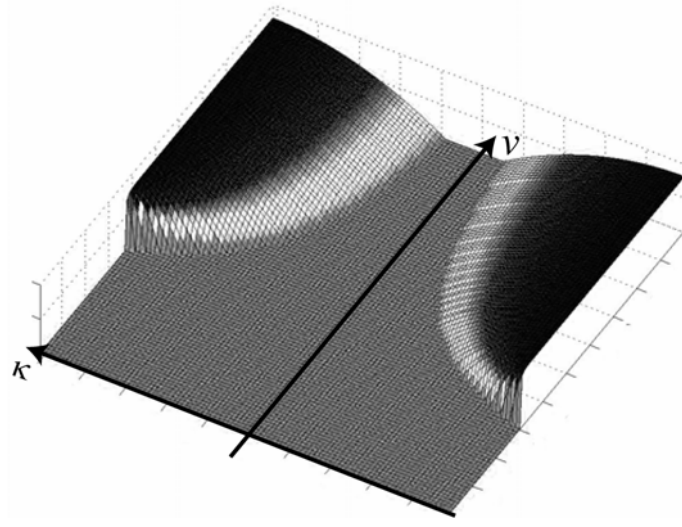


Fig. 3. Illustration of potential function of rollover and side slip constraints.

A corresponding repulsive force is generated as the negative gradient of the repulsive potential, as:

$$\begin{aligned} F_r &= -\nabla PF_r(k, \nu) \\ &= -\nabla_\nu PF_r(k, \nu) - \nabla_\rho PF_r(k, \nu) \end{aligned} \quad (3)$$

where:

$$\begin{aligned} \nabla_\nu PF_r(\kappa, \nu) &= \begin{cases} 4K_r \frac{(\kappa - \kappa_{MAX})^2 (\kappa_r(\nu) + \delta_r)}{\nu(\kappa_r(\nu) - \kappa_{MAX})^3} & \kappa_r < \kappa < \kappa_{MAX} \\ 0 & 0 \leq \kappa < \kappa_r \end{cases} \\ \nabla_\rho PF_r(\kappa, \nu) &= \begin{cases} 2K_r \frac{(\kappa - \kappa_{MAX})}{(\kappa_r(\nu) - \kappa_{MAX})^2} & \kappa_r < \kappa < \kappa_{MAX} \\ 0 & 0 \leq \kappa < \kappa_r \end{cases} \end{aligned} \quad (4)$$

This repulsive force grows increasingly large as the UGV curvature exceeds the maximum allowable curvature defined in equation (1), and is zero otherwise. Thus the

repulsive force affects navigation only when the UGV is on the verge of executing a dynamically inadmissible maneuver due to rollover.

Side slip occurs when the lateral traction forces between a UGV's wheels and the terrain is exceeded by the sum of the centrifugal force and lateral gravitational force component. The maximum path curvature that a UGV can track without excessive side slip can be modeled as follows:

$$\kappa_s(\nu) = \frac{-g_x \pm \mu g_z}{\nu^2} - \delta_s \quad (5)$$

where κ_s is the maximum admissible path curvature. Again, δ_s is introduced for reasons identical to those described above. A potential function is then defined as:

$$PF_s(\kappa, \nu) = \begin{cases} K_s \left(1 - \frac{(\kappa - \kappa_{MAX})^2}{(\kappa_s(\nu) - \kappa_{MAX})^2} \right) & \kappa_s < \kappa < \kappa_{MAX} \\ 0 & 0 \leq \kappa < \kappa_s \end{cases} \quad (6)$$

Again, K_s is a positive gain parameter to modulate the potential function height. An illustration of a potential function for the side slip constraint appears similar to that for the rollover constraint shown in Fig. 3.

A corresponding repulsive force is generated as the negative gradient of the repulsive potential, as:

$$\begin{aligned} F_s &= -\nabla PF_s(\kappa, \nu) \\ &= -\nabla_\nu PF_s(\kappa, \nu) - \nabla_\rho PF_s(\kappa, \nu) \end{aligned} \quad (7)$$

where:

$$\nabla_{\nu} PF_s(\kappa, \nu) = \begin{cases} 4K_s \frac{(\kappa - \kappa_{MAX})^2 (\kappa_s(\nu) + \delta_r)}{\nu(\kappa_s(\nu) - \kappa_{MAX})^3} & \kappa_r < |\kappa| < \kappa_{MAX} \\ 0 & 0 \leq |\kappa| < \kappa_r \end{cases}$$

$$\nabla_{\rho} PF_s(\kappa, \nu) = \begin{cases} 2K_s \frac{(\kappa - \kappa_{MAX})}{(\kappa_s(\nu) - \kappa_{MAX})^2} & \kappa_r < |\kappa| < \kappa_{MAX} \\ 0 & 0 \leq |\kappa| < \kappa_s \end{cases} \quad (8)$$

The repulsive force grows increasingly large as the UGV curvature exceeds the maximum allowable curvature defined in equation (5), and is zero otherwise. Thus the repulsive force affects navigation only when the UGV is on the verge of executing a dynamically inadmissible maneuver due to side slip.

The models employed above are functions of the terrain inclination and traction. An example of the effects of varying inclination on constraint equation (1) can be observed in Fig. 4. Here, rollover constraints are shown for the case of flat terrain, rolling terrain with $\theta = 15^\circ$, and rolling terrain with $\theta = 30^\circ$. The solid or dashed lines indicate the point at which the value of equation (2) exceeds zero. It can be seen that as terrain inclination increases, the rollover constraint model predicts that a UGV can safely execute negative curvature maneuvers (“downslope” turns) at greater velocity than positive curvature maneuvers (“upslope” turns). This is physically reasonable, since during negative curvature maneuvers the gravity vector g_x component acts counter to centripetal acceleration.

An example of the effect of traction on constraint equation (5) can be observed in Fig. 5. Here, side slip constraints are shown for the case of flat terrain, with $\mu = 0.2$, $\mu = 0.6$, and $\mu = 1.0$. The solid or dashed lines indicate the point at which the value of

equation (6) exceeds zero. It can be seen that as terrain traction increases, the side slip constraint model predicts that a UGV can safely execute a fixed-curvature maneuvers at greater velocity. Again, this is physically reasonable, since during travel on high-traction terrain the available cornering force is greater than on low-traction terrain. Thus the proposed potential functions can capture the effects of terrain inclination and traction.

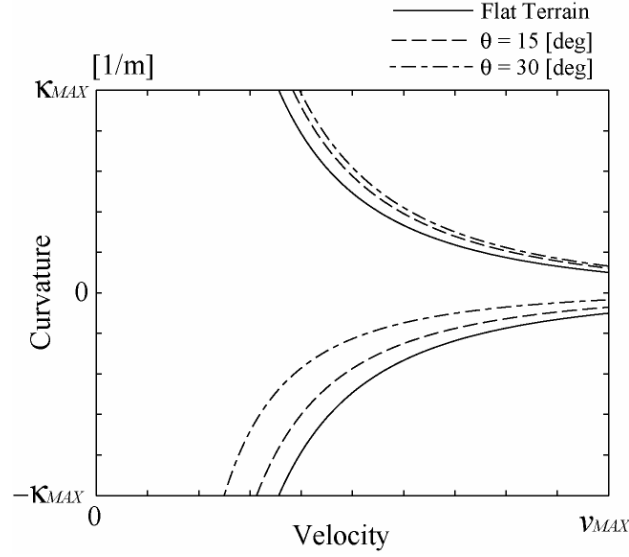


Fig. 4. Illustration of effect of terrain inclination on rollover constraint.

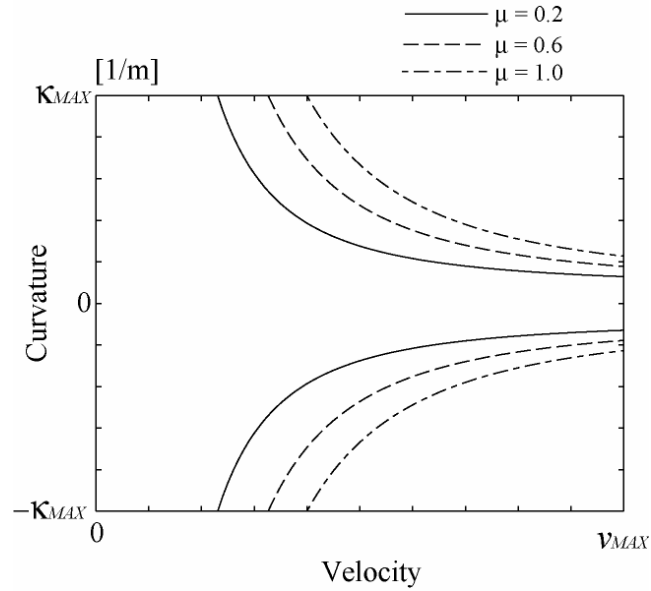


Fig. 5. Illustration of effect of terrain traction on side slip constraint.

Terrain roughness influences rollover and side slip by inducing variation in the wheel normal forces. It has been shown that for natural terrain, the presence of roughness leads to a distribution of curvature-velocity pairs at which rollover or side slip occurs, with the mean of this distribution approximately described by the prediction from the rigid body models of equations (1) and (5) [17, 28]. Monte Carlo simulation methods have been developed for analyzing this distribution as a function of terrain roughness [27, 28]. Detailed discussion of the effects of terrain roughness on UGV mobility are beyond the scope of this paper.

In practice, probability distribution functions related to rollover and side slip can be determined as a function of terrain roughness via off-line Monte Carlo simulation analysis. The parameters δ_r and δ_s can then be chosen to correspond to 3σ limits of these distributions. A look-up table can then be constructed relating δ_r and δ_s to roughness ϖ . Since roughness can be measured on-line in real time, δ_r and δ_s can be modulated to account for roughness. Thus the proposed potential functions can be adapted for in rough terrain scenarios if measurements or estimates of terrain roughness are available.

3.2 *Potential Function for Waypoint Locations*

To enable UGV navigation between waypoints, an attractive potential function is composed with a corresponding attractive force that tends to “pull” the UGV toward the desired waypoint at a given instant. The form of the potential function influences the shape of the resulting UGV path. For example, consider a UGV moving toward a desired waypoint as shown in Fig. 6. Two possible paths to the waypoint are illustrated as paths A and B, resulting from two different potential functions. Both paths possess the same

initial curvature. Path B, however, is more direct and thus more desirable than Path A in the absence of other constraints.

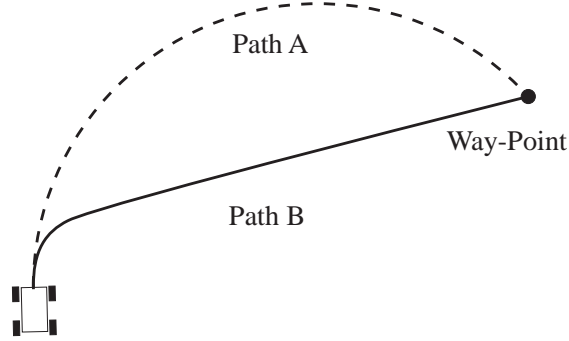


Fig. 6. Comparison of possible UGV paths toward a waypoint.

To generate direct paths between waypoints, a method illustrated in Fig. 7 is proposed. Let O_d be the Euclidean distance between the UGV c.g. and the waypoint. A line connecting the UGV c.g. and waypoint intersects a circle centered at the UGV c.g. with radius $2\kappa_{MAX}$. The desired curvature κ_d to this “virtual waypoint” is taken as the curvature that leads to the intersection point. In the case where $O_d < 2/\kappa_{MAX}$, κ_d is taken as the curvature that leads to the waypoint directly.

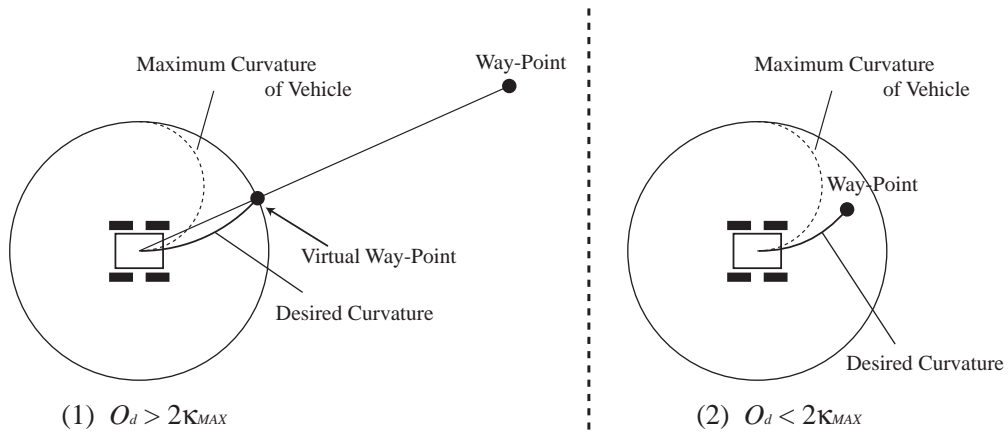


Fig. 7. Computation of desired steering angle using “virtual waypoints.”

A potential function corresponding to the current desired waypoint location is then defined as follows:

$$PF_w(\kappa) = K_w(\kappa - \kappa_d)^2 \quad (9)$$

where K_g is a positive gain parameter to modulate the potential function height. An illustration of a potential function for waypoint location is shown in Fig. 8.

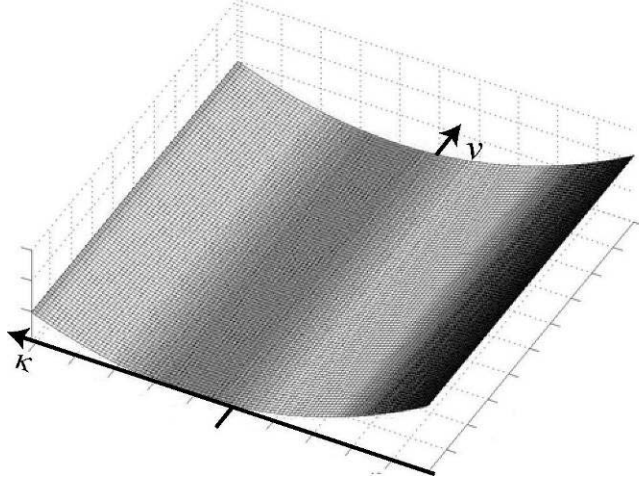


Fig. 8. Illustration of potential function for waypoint location.

A corresponding attractive force is generated as the negative gradient of the attractive potential, as:

$$F_w = -\nabla_{\rho} PF_w(\kappa) \quad (10)$$

where:

$$\nabla_{\rho} PF_w(\kappa, \nu) = 2K_w(\kappa - \kappa_d) \quad (11)$$

The difference in robot trajectories resulting from the use of virtual waypoints is illustrated in a simulation result presented in Section 6.1.

3.3 Potential Function for Desired Velocity

A potential function related to the desired UGV velocity can be simply expressed as follows:

$$PF_v(v) = K_v(v - v_d)^3 \quad (12)$$

where v_d is the desired UGV velocity and K_v is a positive gain parameters to modulate the potential function height. Note that v_d may be a function of position or time to reflect high-level objectives. An illustration of the potential function for the desired velocity is shown in Fig. 9.

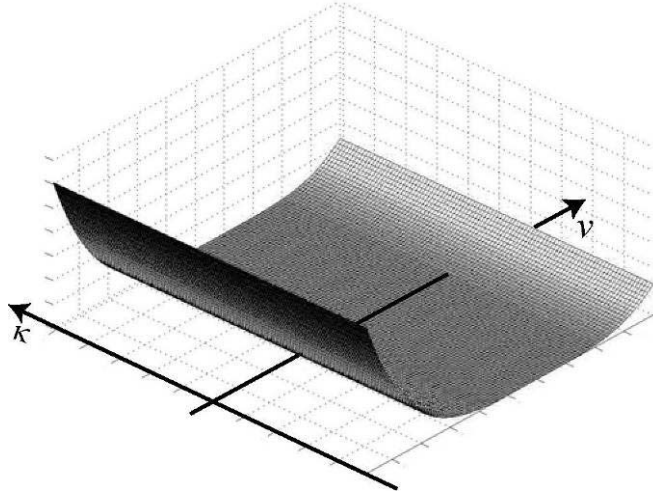


Fig. 9. Illustration of potential function of desired velocity.

A corresponding attractive force is generated as the negative gradient of the attractive potential, as:

$$F_v = -\nabla_v PF_v(v) \quad (13)$$

where:

$$\nabla_v PF_v(\kappa, v) = 3K_v(v - v_d)^2 \quad (14)$$

3.4 Potential Function for Hazard Locations

A potential function related to hazard locations should consider (at minimum) the relative position and orientation of the UGV and hazard(s). Consider the general situation of a UGV approaching a static hazard shown in Fig. 10. Here κ_1 and κ_2 are the maximum and minimum path curvatures toward the hazard from the current UGV position and velocity. A point vehicle representation is assumed and hazard boundaries are computed accordingly.

Here a potential function for hazard location is proposed that considers several factors. First, path curvatures between κ_1 and κ_2 are undesirable if the UGV is near the hazard, yet can be safely employed if the hazard is distant. Second, the potential function value should be higher at high speed than at low speed since both path tracking accuracy and response time decrease with increasing speed. Third, the orientations of hazard(s) relative to the current waypoint (with respect to the UGV position) should influence the hazard potential function value, thus allowing a UGV to “pass” hazards without being unduly disturbed by them. This is illustrated in Fig. 11.

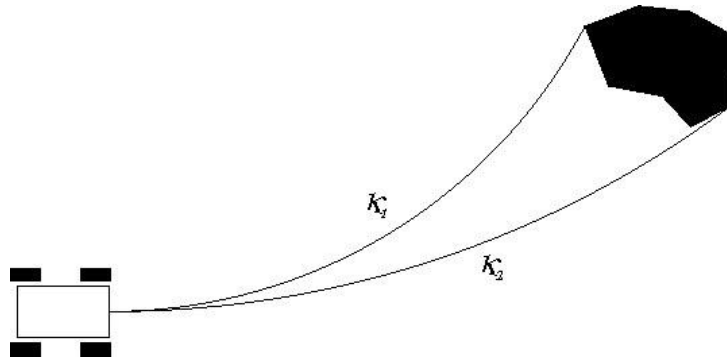


Fig. 10. Minimum and maximum steering angle towards a hazard.

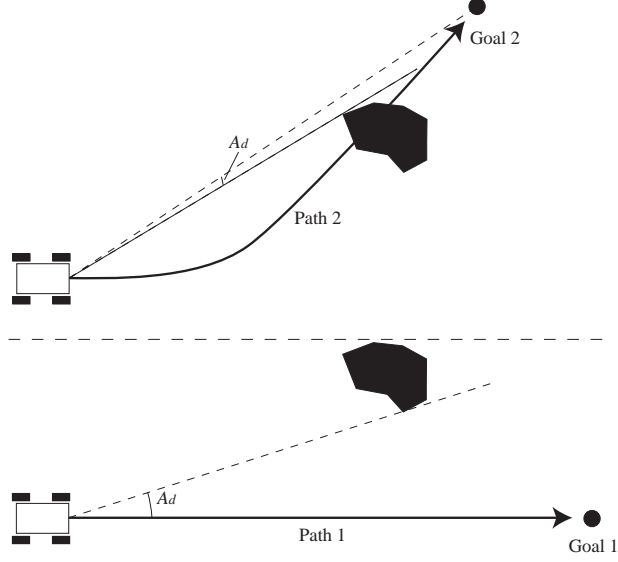


Fig. 11. Influence of relative locations of waypoints and hazards.

From these observations, a potential function for hazard locations is defined as follows:

$$PF_h(\kappa, v) = \frac{K_h(K_{hv}v + 1)}{(K_{hd}O_d + 1)(K_{ha}|A_d| + 1)} e^{-(\kappa - X)^2 / 2\sigma^2} \quad (15)$$

where A_d is the minimum angle between the current waypoint and the hazard of interest (see Fig. 11), $X = (\kappa_1 + \kappa_2)/2$, and $\sigma = (\kappa_1 - \kappa_2)/2$. K_h , K_{hd} , K_{ha} , and K_{hv} are positive gain parameters to modulate the potential function height.

The hazard potential function is chosen as a scaled Gaussian with σ proportional to the hazard “width” as observed by the UGV at a given distance. As the UGV approaches the hazard or travels at increased speed the magnitude of the potential function grows. As the heading angle to the hazard relative to the current waypoint diverges, the magnitude of the potential function diminishes. An illustration of the potential function for a UGV approaching a hazard is shown in Fig. 12. Note that a

single function is employed for each hazard, and multiple hazards can be described as a summation of multiple functions.

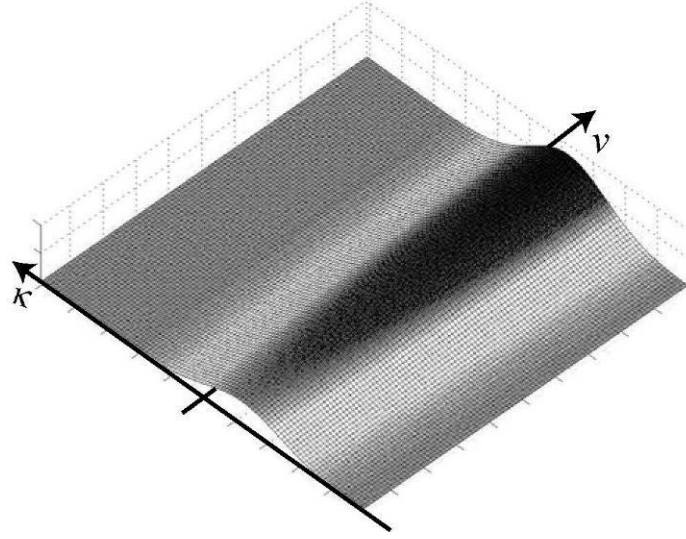


Fig. 12. Illustration of potential function for single hazard location.

A corresponding repulsive force is generated as the negative gradient of the repulsive potential, as:

$$\begin{aligned} F_h &= -\nabla PF_h(\kappa, \nu) \\ &= -\nabla_\nu PF_h(\kappa, \nu) - \nabla_\rho PF_h(\kappa, \nu) \end{aligned} \quad (16)$$

whesre:

$$\begin{aligned} \nabla_\nu PF_h(\kappa, \nu) &= \frac{K_h K_{h\nu}}{(K_{hd} O_d + 1)(K_{ha} | A_d | + 1)} e^{-(\kappa - X)^2 / 2\sigma^2} \\ \nabla_\rho PF_h(\kappa, \nu) &= \frac{K_h (K_{h\nu} \nu + 1)(\kappa - X)}{\sigma (K_{hd} O_d + 1)(K_{ha} | A_d | + 1)} e^{-(\kappa - X)^2 / 2\sigma^2} \end{aligned} \quad (17)$$

3.5 Definition of Net Potential Field

A net potential field is generated as the sum of all proposed potential functions, as:

$$NPF(\kappa, \nu) = PF_r(\kappa, \nu) + PF_s(\kappa, \nu) + PF_w(\kappa) + PF_\nu(\nu) + \sum_{i=1}^n PF_{hi}(\kappa, \nu) \quad (18)$$

where n is the number of hazards present and PF_{hi} is the potential function corresponding to the i^{th} hazard. An illustration of a net potential field is shown in Fig. 13.

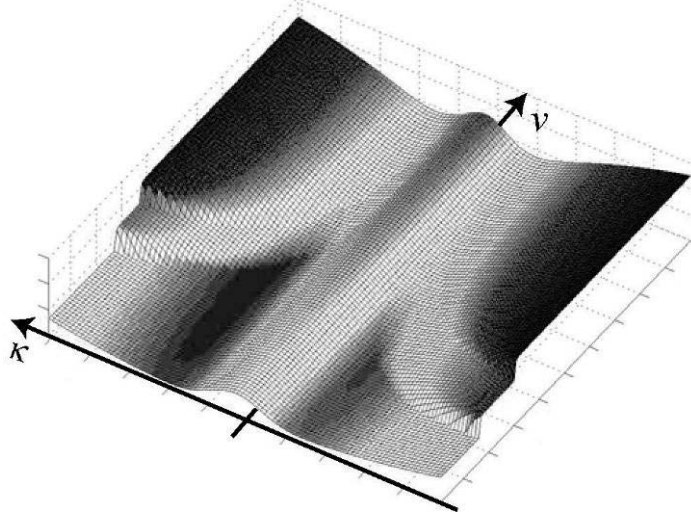


Fig. 13. Illustration of proposed net potential field.

A net force field corresponding to the net potential field is generated as the sum of all proposed virtual forces:

$$NF(\kappa, v) = -\nabla PF_r(\kappa, v) - \nabla PF_s(\kappa, v) - \nabla PF_w(\kappa) - \nabla PF_v(v) - \sum_{i=1}^n \nabla PF_{hi}(\kappa, v) \quad (19)$$

4. Navigation Algorithm Description

During navigation, the gradient of the net potential field is computed at the UGV's position in the trajectory space (i.e. its instantaneous path curvature and longitudinal velocity $\tau = (\kappa, v)$). A desired curvature and velocity is then chosen in the direction of maximum descent as $\tau^* = \tau + NF(\tau)$. The desired maneuver τ^* is used to derive command inputs for low-level control of UGV steering angle and throttle. This procedure is repeated at a control rate appropriate to the navigation task, usually 1-10 Hz.

Three factors must be considered during implementation of the proposed algorithm. First, not all regions of TS are reachable in a finite time t due to limits on UGV acceleration, deceleration, and steering rate. Thus τ^* should be chosen in a subspace of TS termed the “reachable trajectory space” [20]. Second, calculation of the potential functions in equation (18) may be corrupted by sensor noise, and thus filtering should be performed during the gradient calculations in equation (19). Third, the desired path curvature and velocity must be mapped to steering angle and throttle command inputs to perform low-level control. These factors are discussed below.

4.1 Reachable Trajectory Space Description

The reachable trajectory space is computed based on knowledge of the UGV’s instantaneous curvature and velocity, and its acceleration, braking, and steering characteristics. For a UGV located at τ in the trajectory space, an estimate of the maximum and minimum attainable velocities in a time t is:

$$\begin{aligned} v_{reachable}^{\max} &= v + a^+ t \\ v_{reachable}^{\min} &= v - a^- t \end{aligned} \quad (20)$$

where a^+ and a^- are UGV acceleration/deceleration parameters, respectively, assuming constant acceleration/deceleration capability. The maximum and minimum attainable path curvatures for a front-wheel steered vehicle in time t are:

$$\begin{aligned} \kappa_{reachable}^{\max}(v) &= \kappa + \dot{\kappa}_{\max} t \\ \kappa_{reachable}^{\min}(v) &= \kappa - \dot{\kappa}_{\max} t \end{aligned} \quad (21)$$

where $\dot{\kappa}_{\max}$ is the maximum rate of change of path curvature. This parameter can be computed from the single-track vehicle model shown in Fig. 14 [29]. In this model the

properties of the front and rear wheel pairs are lumped into single front and rear wheels located on the centerline of the vehicle, and:

$$|\dot{\kappa}_{\max}| = \frac{\tan \dot{\delta}_{\max}}{L} \quad (22)$$

where $\dot{\delta}_{\max}$ is the maximum rate of change of the UGV steering angle. Fig. 15 shows an example of the reachable trajectory space.

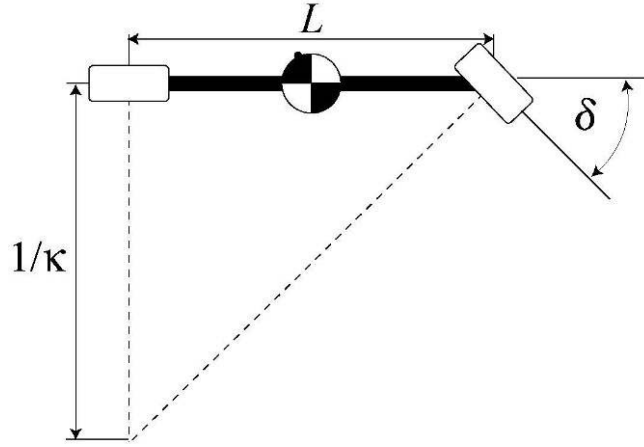


Fig. 14. Single-track UGV model for reachable trajectory space calculation.

4.2 Potential Field Gradient Calculation

In practical application of the proposed algorithm the calculation of the potential functions in equation (18) will be corrupted by sensor noise, and thus filtering must be performed during the gradient calculations in equation (19). Here a plane-fitting approach is proposed to compute the potential field gradient. This approach was chosen due to its computational efficiency and ability to mitigate the potentially significant effects of noise on the gradient calculation.

In the proposed approach the reachable trajectory space, which is nominally rectangular, is discretized into nine equal-area rectangular regions. Other discretization geometries and resolutions are possible, however this discretization was found to yield

good results in simulation and experimental trials. A maneuver is chosen via the following algorithm:

1. The value of the net potential field at the center of each region is calculated from equation (18) (see Fig. 15(a-b));
2. A plane fit to the potential field values is calculated and the gradient of the plane is computed (see Fig. 15(c)). The direction of maximum descent is taken as the desired maneuver direction;
3. The desired maneuver τ^* is chosen as the point on the boundary of the reachable trajectory space in the direction of the desired maneuver from the current point.

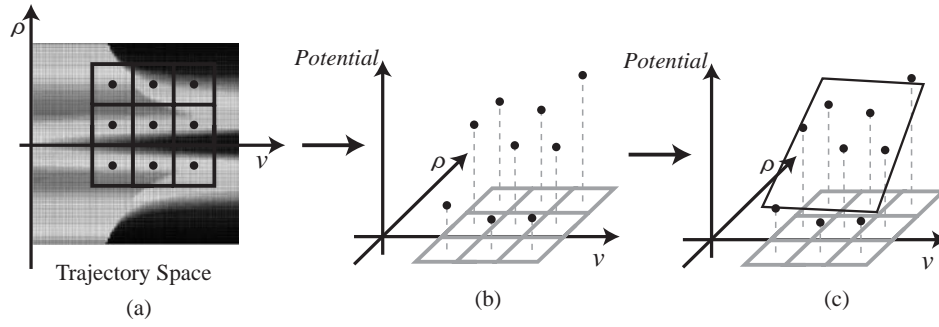


Fig. 15. Illustration of gradient calculation algorithm.

4.3 Command Input Calculation

To perform low-level control of the UGV, the desired maneuver τ^* is mapped to a pair of command inputs for the UGV steering angle and throttle setpoint. Assuming a single-track vehicle model (see Fig. 14), steering angle can be computed from path curvature as:

$$\delta = \tan^{-1}(L\kappa) \quad (23)$$

The desired maneuver velocity can be used directly as a low-level control setpoint, assuming a velocity-controlled vehicle. A variety of low-level control laws can

then be employed to track the desired curvature and velocity. In this work simple PD compensators were employed.

5. Local Minimum Problem Discussion

5.1 Conventional Local Minimum Description

The existence of local minima is a fundamental problem associated with potential fields constructed from multiple potential functions. A classical local minimum situation for Cartesian space potential field methods is illustrated in Fig. 16. Due to the interaction of the repulsive and attractive potential functions associated with the hazard and goal, Area A is a possible location of a local minimum. In Cartesian space potential field applications, this would result in the robot stopping in Area A and not the goal location.

A second situation is shown in Fig. 17. Here the goal is located between the UGV and a hazard, and the waypoint lies within the region of influence of the hazard potential function. In this case the global minimum of the potential field is not the waypoint position. A UGV might reach this global minimum yet not reach the waypoint. This situation is called a “free-path local minimum.”

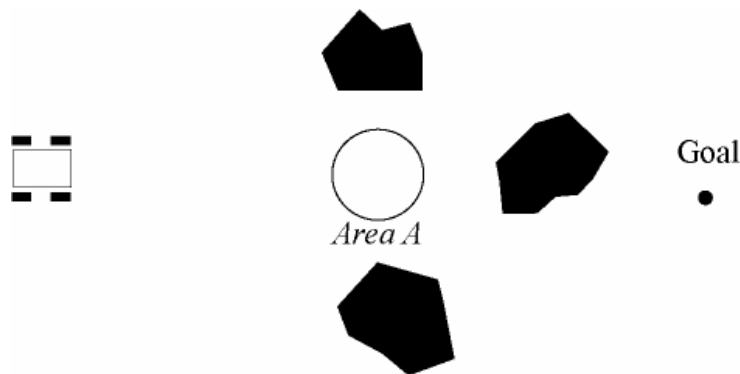


Fig. 16. Example of conventional local minimum.



Fig. 17. Example of conventional free-path local minimum.

5.2 Trajectory Space Local Maximum and Minimum Description

Situations that lead to local minimum situations in classical potential field approaches often lead to local maximum situations in the proposed method. For example, Fig. 18 shows a situation similar to that shown in Fig. 16, with a corresponding trajectory space potential field. In this situation $\tau = (0, v_d)$, $\kappa_d = 0$, $X = 0$, $A_d = 0$, $\theta = \phi = 0^\circ$, and $\mu = 1.0$. Thus only the hazard potential function influences computation of τ^* . In this situation the hazard potential function of equation (15) becomes:

$$PF_h(\kappa, v) = \frac{K_h(K_{hv}v + 1)}{K_{hd}O_d + 1} e^{-\kappa^2/2\sigma^2} \quad (24)$$

and $\nabla_\rho PF_h(0, v_d) = 0$. Thus the symmetry of the hazard potential function causes the potential field gradient to be zero in the curvature dimension, and the desired maneuver directs the UGV toward the hazard.

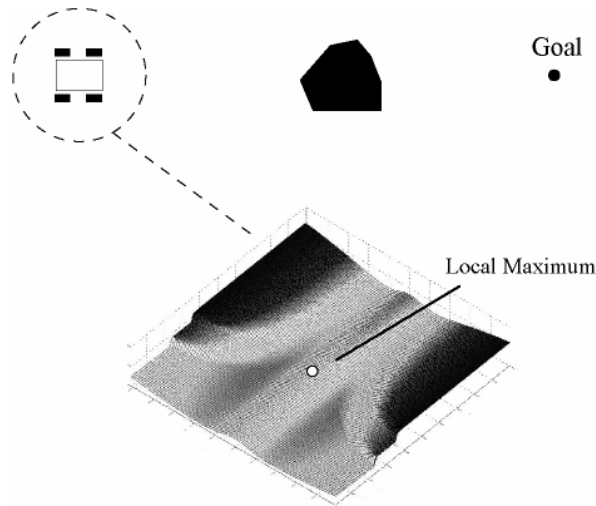


Fig. 18. Example of trajectory space local maximum.

Local maxima are unlikely to occur in practice since sensor noise, terrain unevenness, and terrain inclination all tend to introduce asymmetry to the net potential field. However, to address this issue Gaussian random noise of small amplitude is added to each element of the net potential field during the algorithm described in Section 4.2. This method serves to perturb unstable local maxima, and avoid situations such as that shown in Fig. 18. It has been observed empirically that the addition of a small amount of random noise does not degrade navigation performance.

An example of the effect of this method is shown in Fig. 19. Here a situation similar to that shown in Fig. 16 is presented. In this case, however, the addition of noise causes the UGV to be perturbed from the (unstable) local maxima in the trajectory space, and select a maneuver that leads to successful navigation to the goal.

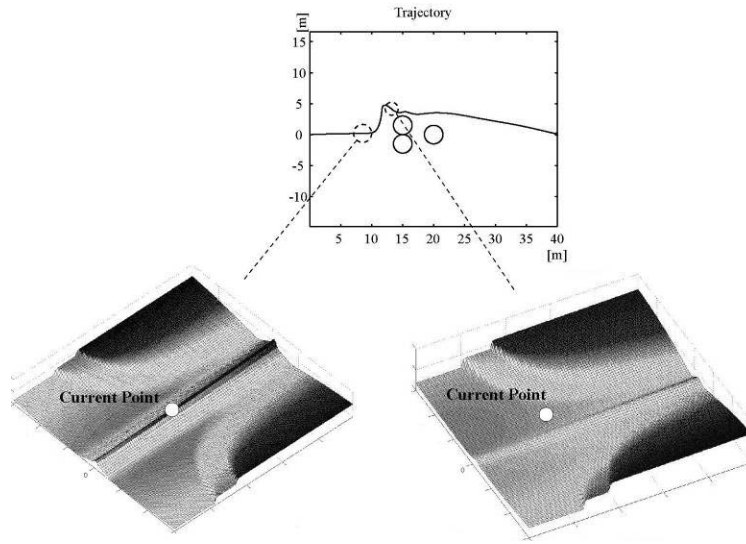


Fig. 19. Example of local maximum avoidance by addition of noise.

The existence of local minima is possible when a UGV encounters multiple hazards. In contrast to Cartesian space methods, a trajectory space local minima does not

result in the UGV stopping at a location that is not the goal location (save for cases where $v = 0$). Rather, the UGV continues to move at the curvature and velocity corresponding to the local minima point. Thus the trajectory space net potential function is continually changing, even if the UGV is “trapped” in a local minima.

As has been noted by previous researchers, a simple method for addressing these situations is to continue moving according to the total virtual force until the relative positions of the hazards has eliminated the existence of the local minimum [7]. Since the potential function is continually changing it is highly likely that the local minima will migrate or vanish over time. Though simple, this “waiting” method has been found to be effective in practice.

Another potential type of local minimum that can occur is a limit cycle, where the vehicle follows the same trajectory permanently, usually due to the presence of dense obstacles. Methods for avoiding such limit cycles have been developed by previous researchers [32].

6. Simulation Results

Simulations were conducted of a small four-wheeled UGV traveling at high speeds over uneven terrain using Matlab and the dynamic simulation software ADAMS 12.0. ADAMS is a multibody simulation engine that allows simulation of high d.o.f. systems on uneven terrain. The UGV was modeled as a front-wheel steered vehicle with a mass of 3.1 kg and independent spring-damper suspensions with linear stiffness and damping parameters $k = 500.0$ N/m and $b = 110$ Ns/m, respectively. The UGV length $L = 0.27$ m, the half-width $d = 0.124$ m, the height of UGV c.g. from ground $h = 0.055$ m, and the wheel diameter was 0.12 m.

Wheel-terrain contact forces were derived from the magic tire model using standard parameters for a passenger vehicle tire operating on asphalt [30]. This model is generally accepted for modeling on-road mobility, and was assumed to be a reasonable model for off-road mobility when soil deformation is small. Terrain roughness was created using fractal techniques, with fractal number of 2.05, grid spacing of 2 wheel diameters, and height scaling of 35 wheel diameters [18]. This corresponds to flat but bumpy terrain. Potential function gain parameters were chosen empirically to balance the relative contributions of the various potential functions to the net potential field. The parameter values were set as follows: $K_r = 800$, $K_s = 800$, $K_w = 0.3$, $K_v = 0.5 \times 10^{-5}$, $K_h = 1500$, $K_{hd} = 0.05$, $K_{ha} = 10$, $K_{hv} = 0.07$. These parameters were derived from analysis of simulation studies. Good performance of the algorithm was observed to exist across a range of parameters.

6.1. *Effect of Virtual Waypoints*

Fig. 20 shows a simulation result illustrating the effect of using virtual waypoints (see Subsection 3.2). Here the UGV began at $(x,y)=(0.0,0.0)$ and a single waypoint was set at $(x,y) = (15.0,15.0)$. Paths resulting from the use of virtual waypoints are in general more direct than paths resulting from widely-spaced user-defined waypoints. In this result, the total length of the trajectory employing virtual waypoints was 21.4 m compared to 22.8 m without using virtual waypoints.

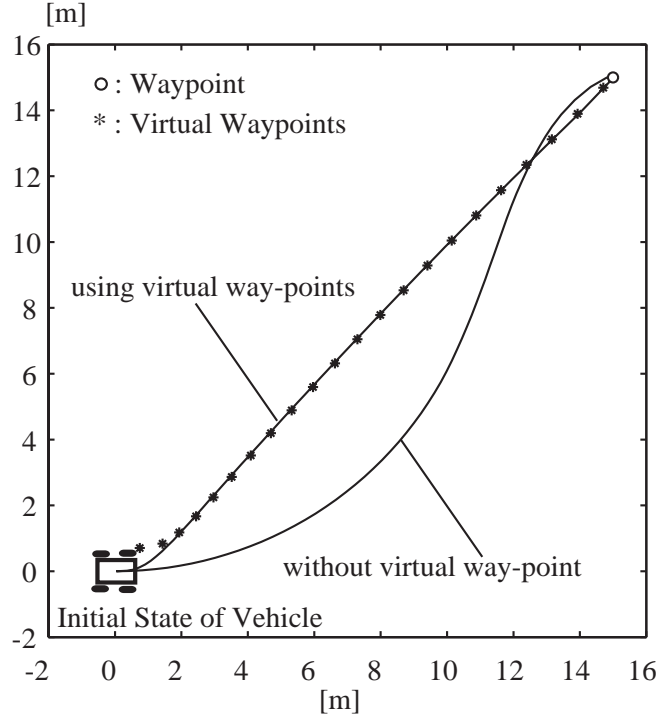


Fig.20. Influence of Virtual Waypoint

6.2. Obstacle Avoidance and Way-Point Navigation

Numerous simulations were performed to study the algorithm's ability to guide a UGV at high speed among multiple waypoints while avoiding multiple hazards on flat terrain. Results from a representative simulation are shown in Figs. 21-23. Here the UGV began at $(x,y) = (0.0, 0.0)$, hazards were set at $(x,y) = \{(15.0, 0.0), (50.0, 22.0)\}$ and waypoints were set at $(x,y) = \{(30.0, 0.0), (40.0, 20.0), (60.0, 20.0)\}$. PD control was employed for steering angle and velocity control. The desired velocity during this simulation was 5.0 m/s. For this small vehicle at this speed, both rollover and significant side slip were possible.

Fig. 21 shows the UGV Cartesian space trajectory and shape of the potential field at two locations. The vehicle safely navigated between three waypoints while avoiding two hazards. Fig. 22 shows that the velocity remained near the desired value of 5.0 m/s

except during turns of large curvature (points (a), (b), and (c)). During these turns the rollover and/or side slip potential functions caused the velocity to decrease in order to avoid a dynamically inadmissible maneuver. Fig. 23 shows plots of the UGV roll angle and slip angle during the trajectory. Slip angle refers to the difference of the angle between the UGV velocity vector at the c.g. and the longitudinal axis of the vehicle. Due to the UGV's relatively high speed the maximum values of roll angle and slip angle are large, but did not lead to a dynamically inadmissible maneuver.

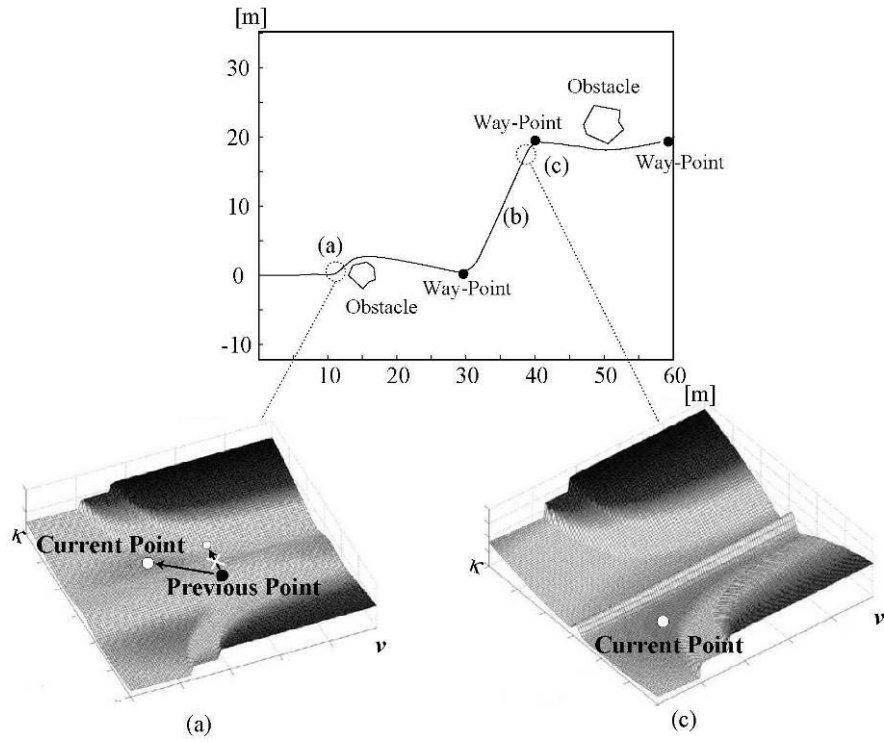


Fig. 21. Map and sample trajectory spaces of simulation result.

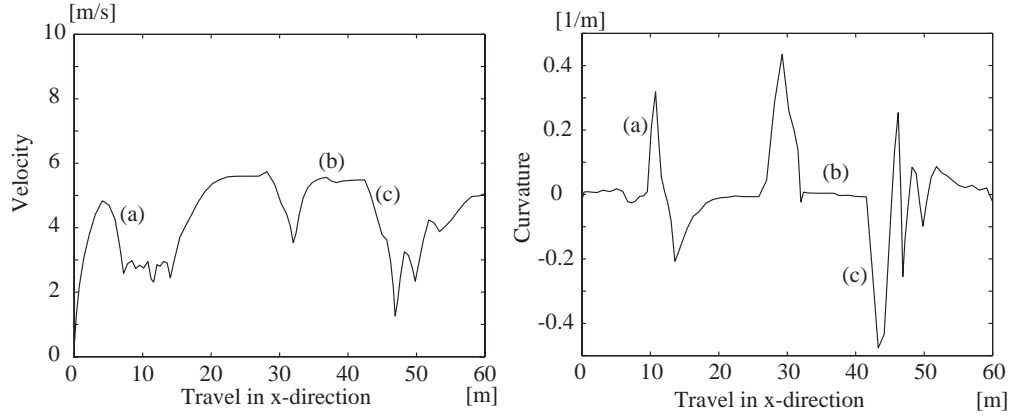


Fig. 22. UGV velocity and curvature—simulation results.

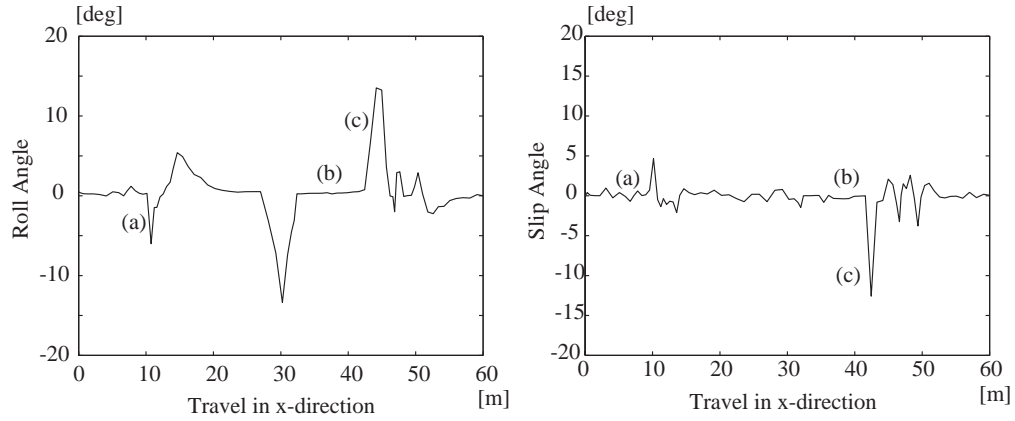


Fig. 23. UGV Roll angle and slip angle—simulation results.

6.3 *Effect of Velocity on Navigation*

Simulations were performed to study the effect of desired UGV velocity on algorithm performance. A map of a representative simulation is shown in Fig. 24. Hazards are located at $(x,y) = \{(25.0, 0.0), (40.0, 2.0)\}$ and waypoints are set at $(x,y) = \{(50.0, 0.0), (70.0, 0.0)\}$. Vehicle and terrain parameters were identical to those in the simulation in Section 6.1.

Simulation results are shown in Fig. 25 and 26 for the case where desired UGV velocity was 5.0 m/s. As in the simulations of Section 6.1 the UGV velocity decreased at regions of large path curvature in order to avoid dynamically inadmissible maneuvers. The UGV safely navigated between two waypoints while avoiding two hazards.

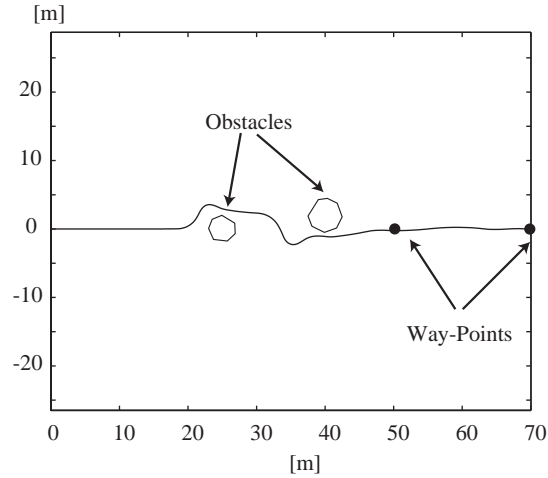


Fig. 24. Map and trajectory of simulation result for desired velocity of 5.0 m/s

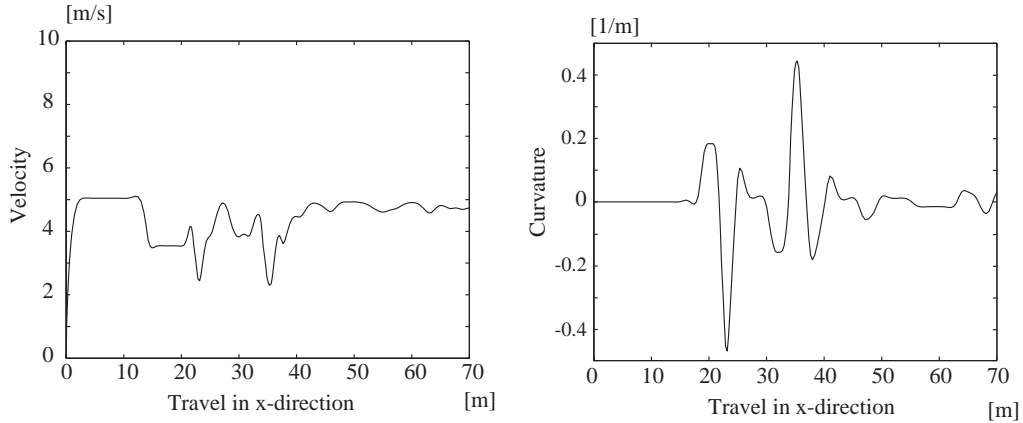


Fig. 25. UGV Velocity and curvature for desired velocity of 5.0 m/s

In contrast, Fig. 27 and 28 shows results from a simulation of a UGV traveling through identical terrain with the same hazard and waypoint locations, now with a desired

velocity of 7 m/s. In this case the UGV successfully skirted both of the hazards and reached both waypoints. The overall path differed significantly from the previous simulation, however, due to the increased speed of the UGV and the correspondingly reduced achievable path curvature. However, the UGV safely navigated at a relatively high speed while avoiding rollover or significant side slip.

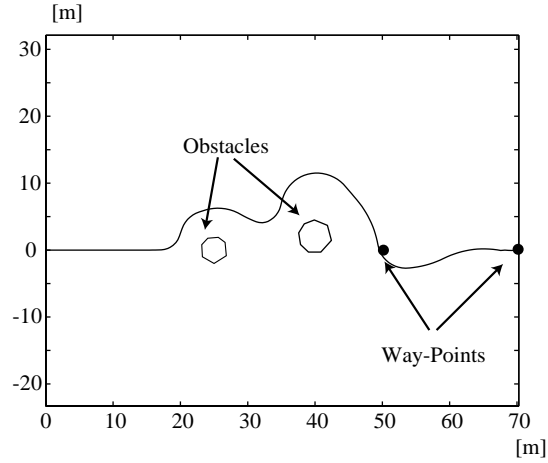


Fig. 26. Map and trajectory of simulation result for desired velocity of 7.0 m/s

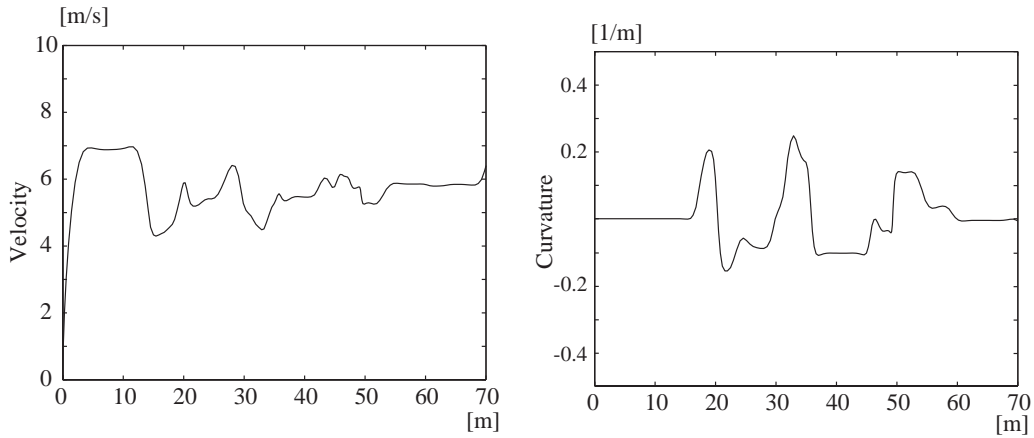


Fig. 27. UGV Velocity and curvature for desired velocity of 7.0 m/s

6.4 Effect of Terrain Inclination on Algorithm Performance

Simulations were performed to study the effect of terrain inclination on algorithm performance. An illustration of the scenario is shown in Fig. 28. The hazard and waypoint locations are identical to those in the scenario presented in Section 6.2, however here the terrain was inclined at a roll angle of 20° with respect to the UGV's initial orientation. Vehicle and terrain parameters were identical to those in the previous simulations. The desired UGV velocity was 5.0 m/s.

Simulation results are shown in Figs. 29 and 30. The resulting UGV trajectory shown in Fig. 29 differs significantly from the flat-terrain case (see Fig. 24) due to the effect of terrain inclination on trajectory space rollover and side slip constraints. As expected, the UGV executed a safe “downslope” maneuver due to potential field asymmetry caused by terrain inclination. As in the simulations of Section 6.1, UGV velocity decreased at regions of large path curvature to avoid dynamically inadmissible maneuvers (see Fig 30). This result highlights the algorithm’s ability to safely navigate a UGV even on steeply inclined terrain.

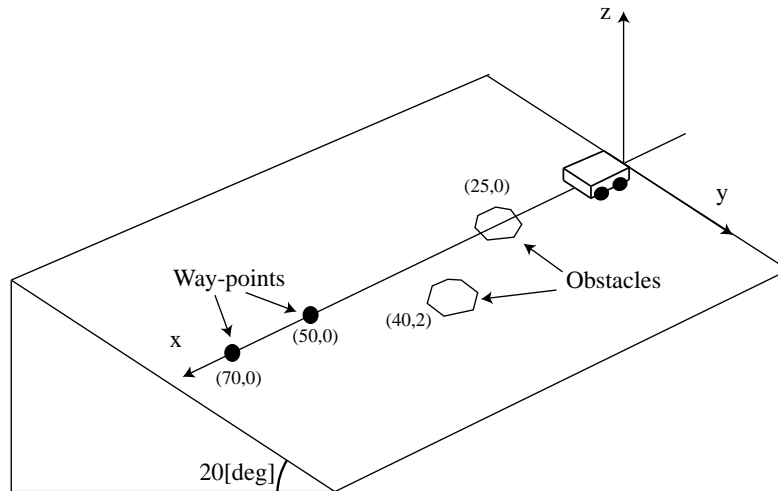


Fig.28. Illustration of scenario for terrain inclination analysis

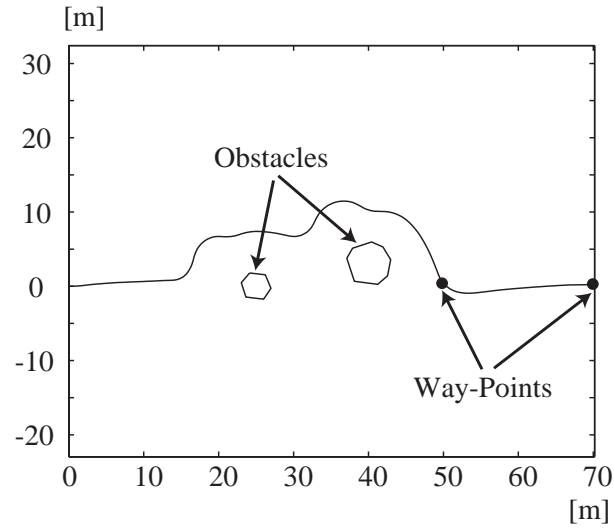


Fig.29. Trajectory of simulation result for terrain inclination of 20°

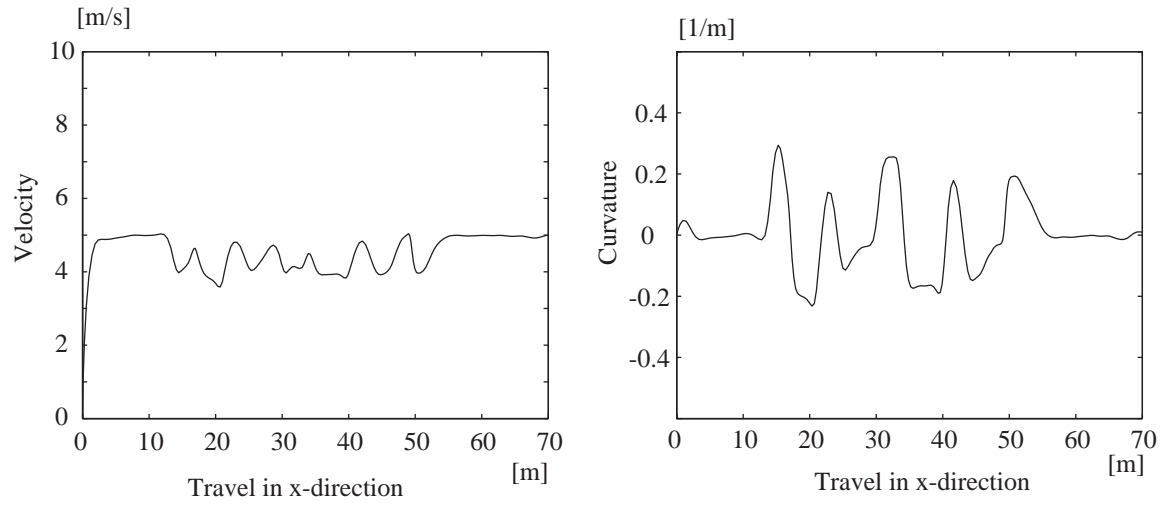


Fig.30. UGV Velocity and curvature for terrain inclination of 20°

7. Experimental Results

A limited number of proof-of-concept experiments were performed to study the algorithm's effectiveness in rough, natural terrain. Experiments were performed on the UGV ARTEMIS, shown in Fig. 31 [20]. ARTEMIS is a four wheeled front-wheel steered vehicle equipped with a Zenoah G2D70 gasoline engine, 700 MHz Pentium III PC -104 onboard computer, Crossbow AHRS-400 INS, a tachometer to measure wheel angular velocity, 20 cm resolution DGPS, and Futaba steering and throttle control servos. The UGV length $L = 0.56$ m, the half-width $d = 0.29$ m, the height of UGV c.g. from ground $h = 0.26$ m, and the wheel diameter was 0.25 m. The body mass was 28.0 kg and the mass of each wheel was 1.85 kg. Experiments were conducted on flat, bumpy terrain covered with grass with an estimated $\mu = 0.8$. In each experiment, the UGV initial position was the origin of the inertial frame, with initial heading aligned with the x axis. Unfortunately due to hardware malfunctions only a limited number of experiments were performed.

First experiments were conducted to study high speed hazard avoidance. A hazard with 1.0 m radius was set at $(x,y) = (15.0, 0.0)$ and a waypoint was set at $(x,y) = (30.0, 0.0)$. The desired velocity was set at 4.0 m/s. For the ARTEMIS UGV, rollover can occur at speeds above 3.5 m/s.



sFig. 31. ARTEMIS experimental UGV on outdoor terrain.

Results from the experiment are shown in Figs. (32-34). The UGV trajectory is shown in Fig. 32. It can be seen that the UGV successfully avoided the hazard and reached the waypoint. UGV velocity and curvature profiles are shown in Fig. 33. The UGV roll angle profile is shown in Fig. 34. As in the simulation studies, the velocity decreased at periods of large curvature (i.e. around $x = 15.0$ m) and was controlled to near 4.0 m/s in hazard-free regions (i.e. after $x = 25.0$ m). Finally, the vehicle navigated without rollover or side slip. Each computation cycle, involving construction of the net potential field and selection of a maneuver, required approximately 50 ms.

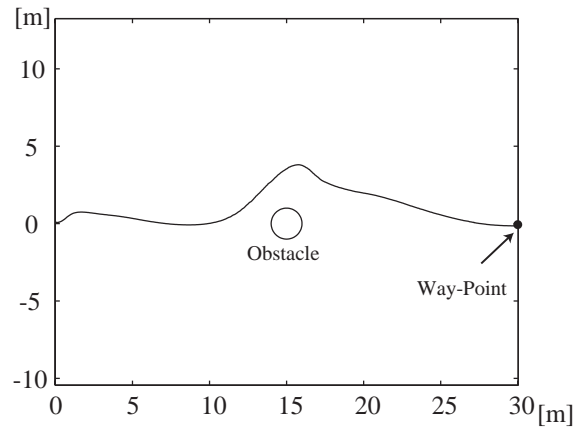


Fig. 32. GPS Trajectory of hazard avoidance experiment.

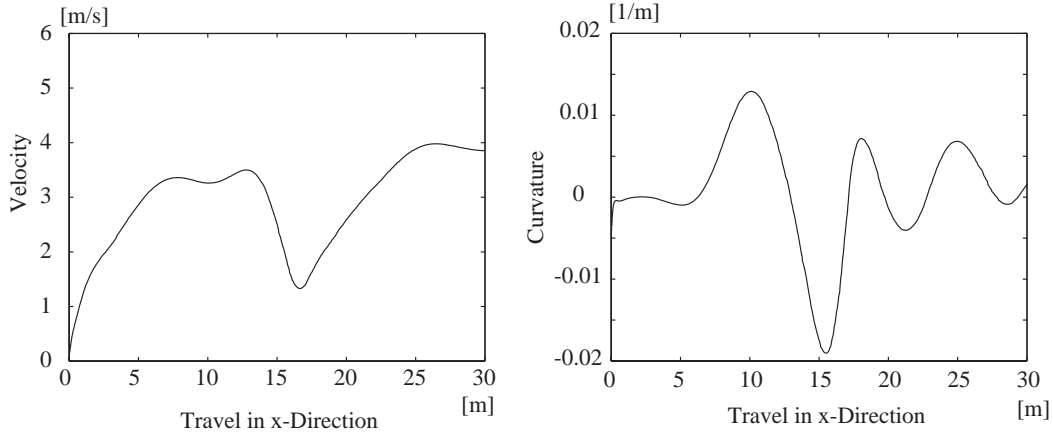


Fig. 33. Velocity and curvature of hazard avoidance experiment.

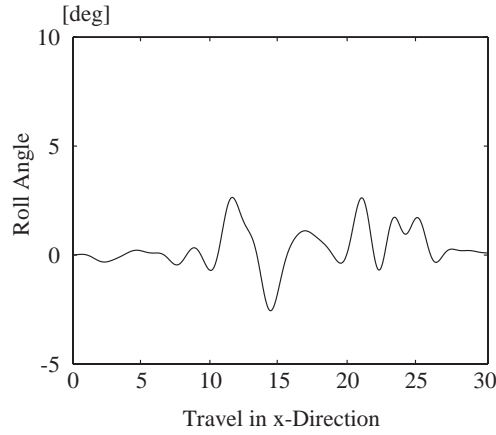


Fig. 34. UGV roll angle of hazard avoidance experiment.

Other experiments were conducted to study high speed navigation between multiple waypoints. Three waypoints were set at $(x,y) = \{(25.0, 0.0), (30.0, 10.0), (40.0, 10.0)\}$. The desired velocity was 4.0 m/s. The target waypoint was indexed when the UGV moved to within 2.0 m of the current waypoint. An experimental result is shown in Figs. (35-37). Fig. 35 shows that the vehicle successfully navigated between waypoints and reached the goal location. Fig. 36 shows that the velocity was controlled near 4.0 m/s, and decreased during periods of large curvature. The UGV roll angle profile is shown in Fig. 37. Again, the vehicle navigated without rollover or side slip. These

results suggest that the proposed method can be used for real time navigation of a UGV at high speeds.

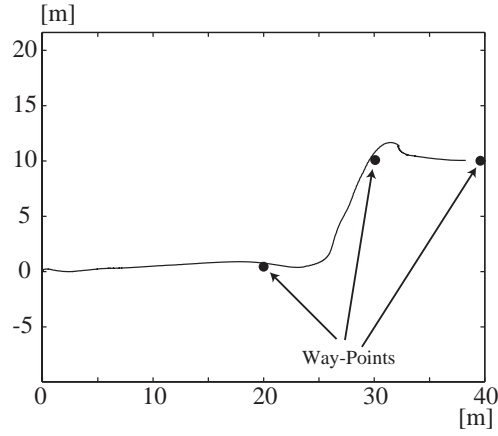


Fig. 35. Trajectory of waypoints navigation experiment.

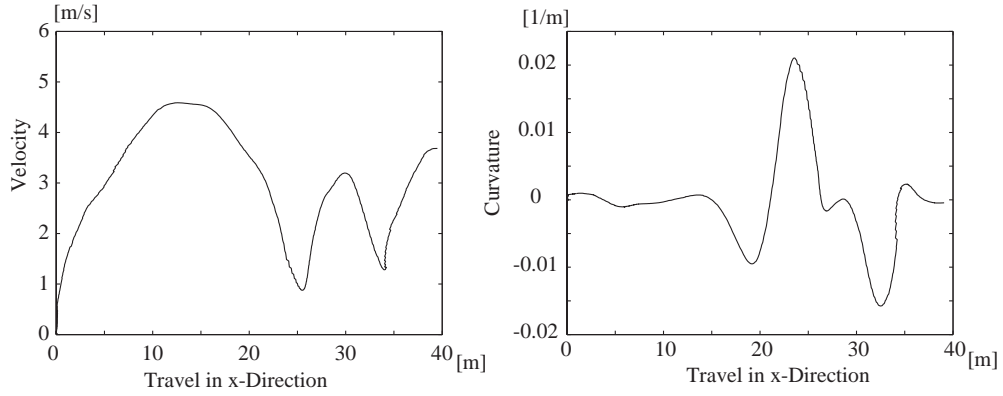


Fig. 36. Velocity and curvature of waypoint navigation experiment.

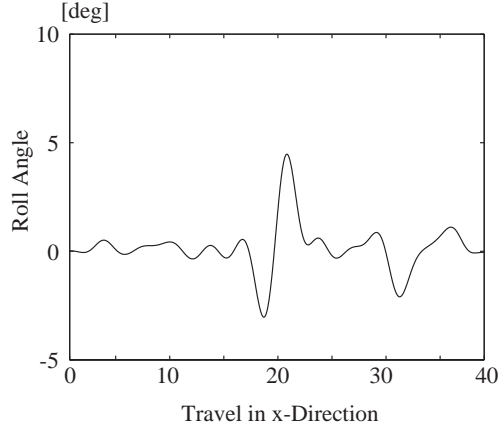


Fig. 37. UGV roll angle of waypoint navigation experiment.

8. Conclusions

This paper has presented a novel potential field-based method for high speed navigation of UGVs on rough terrain. The potential field is constructed in the trajectory space defined by a UGV instantaneous path curvature and longitudinal velocity. Dynamic constraints, terrain conditions, and navigation conditions can be expressed in the proposed potential field framework. A maneuver is chosen within a set of performance bounds, based on the local potential field gradient. Issues related to local minima and maxima were discussed, and it was shown that a simple randomization technique can be employed to address these problems. Simulation and experimental results demonstrated the effectiveness of the method in rough, natural terrain. The method is computationally efficient, and thus suitable for on-board real-time implementation. Current research involves experimental validation of the method on highly rough outdoor terrain.

Acknowledgments

The authors would like to thank Matthew Spenko for his assistance in performing the experiments presented in this paper. This research was supported by the U.S. Army

Research Office, the U.S. Army Tank-automotive and Armaments Command and the Defense Advanced Research Projects Agency.

References

- [1] J. Walker, "Unmanned Ground Combat Vehicle Contractors Selected," *DARPA News Release*, February 7, 2001, (www.darpa.mil)
- [2] G. Gerhart, R. Goetz, D. Gorsich, "Intelligent Mobility for Robotic Vehicles in the Army after Next," *Proceedings of the SPIE Conference on Unmanned Ground Vehicle Technology*, 1999
- [3] Z. Shiller and J. Chen, "Optimal Motion Planning of Autonomous Vehicles in 3-Dimensional Terrains," *Proceedings of the IEEE International Conference on Robotics and Automation*, pp.198-203, 1990
- [4] A. Kelly, and A. Stentz, "Rough Terrain Autonomous Mobility – Part 1: A Theoretical Analysis of Requirements," *Autonomous Robots*, Vol. 5, pp.129-161, 1998
- [5] O. Khatib, "Real-time Obstacle Avoidance for Manipulators and Mobile Robots," *International Journal of Robotics Research*, Vol. 5, No. 1, pp. 90-98, 1986
- [6] J. Barraquand and B. Langlois and J. Latombe, "Numerical Potential Field Techniques for Robot Path Planning," *IEEE Trans. on Systems, Man, and Cybernetics*, Vol. 22, No.2, pp. 224-241, 1992
- [7] S. Ge and Y. Cui, "Dynamic Motion Planning for Mobile Robots Using Potential Field Method," *Autonomous Robots*, Vol. 13, 2002

- [8] S. Caselli, M. Reggiani, and R. Sbravati, "Parallel Path Planning with Multiple Evasion Strategies," *Proceedings of the IEEE International Conference on Robotics and Automation*, pp. 1232-1237, 2002
- [9] H. Tanner, S. Loizou, and K. Kyriakopoulos, "Nonholonomic Navigation and Control of Cooperating Mobile Manipulators," *IEEE Transaction on Robotics and Automation*, Vol. 19, No. 1, 2003
- [10] B. Hussien, "Robot path planning and obstacle avoidance by means of potential function method", *Ph.D Dissertation*, University of Missouri-Columbia, 1989.
- [11] E. Rimon and D.E. Koditschek, "Exact robot navigation using artificial potential functions", *IEEE Transactions on Robotics and Automation*, Vol. 8, No. 5, 501–518, 1992.
- [12] K.J. Kyriakopoulos, P. Kakambouras and N.J. Krikelis, "Navigation of Nonholonomic Vehicle in Complex Environments with Potential Field and Tracking", *Proceedings of the IEEE International Conference on Robotics and Automation*, pp. 3389-3394, 1996
- [13] R.A. Conn and M. Kam, "Robot motion planning on N-dimensional star worlds among moving obstacles", *IEEE Trans. Robot. Autom.*, Vol. 14, No. 2, 320–325, 1998.
- [14] J.H. Chuang, N. Ahuja, "An analytically tractable potential field model of free space and its application in obstacle avoidance", *IEEE Trans. Sys. Man, Cyb.—Part B: Cyb*, Vol. 28, No. 5, 729–736, 1998.

- [15] H. Haddad, M. Khatib, S. Lacroix and R. Chatila., "Reactive Navigation in Outdoor Environments using Potential Fields," *Proceedings of the Intl. Conf. on Robotics and Automation*, pp. 1232-1237, 1998
- [16] D. Fox, W. Burgard and S. Thrun, "The Dynamic Window Approach to Collision Avoidance," *IEEE Robotics and Automation Magazine*, Vol.4, No.1, 23-33, 1997
- [17] O. Brock and O. Khatib, "High-Speed Navigation Using the Global Dynamic Window Approach," *IEEE International Conference on Robotics and Automation*, 341-346, 1999
- [18] P. Ogren and N. Leonard, "A Convergent Dynamic Window Approach to Obstacle Avoidance," *IEEE Transactions on Robotics*, Vol. 21, 188-195, 2005
- [19] M. Spenko, K. Iagnemma, and S. Dubowsky, "High Speed Hazard Avoidance for Mobile Robots in Rough Terrain," *Proceedings of the SPIE Conference on Unmanned Ground Vehicles*, 2004
- [20] M. Spenko, *Hazard Avoidance for High Speed Rough Terrain Unmanned Ground Vehicles*, Ph.D. Thesis, Massachusetts Institute of Technology, 2005
- [21] Anthony Stentz, "The NAVLAB System for Mobile Robot Navigation," *Carnegie Mellon University Ph.D. Thesis, School of Computer Science* CMU-CS-90-123, March, 1990.
- [22] Dudgeon, J. and Gopalakrishnan, R. "Fractal-based modeling of 3D terrain surfaces." *Proc. of the IEEE Conference on Bring Together Education, Science, and Technology*, 1996.

- [23] Arakawa, K., and Krotkov, E. "Estimating Fractal Dimension from Range Images of Natural Terrain." Technical Report CMU-CS-91-156, School of Computer Science, Carnegie Mellon University, Pittsburgh, PA, July 1991
- [24] Iagnemma, K., and Dubowsky, S., *Mobile Robots in Rough Terrain*, STAR Series on Advanced Robotics, Springer, 2004.
- [25] K. D. Iagnemma and S. Dubowsky, "Terrain Estimation for High Speed Rough Terrain Autonomous Vehicle Navigation," in *Proc. SPIE Conf. Unmanned Ground Vehicle Technology IV*, 2002.
- [26] P. Bellutta, R. Manduchi, L. Matthies, K. Owens, and A. Rankin, "Terrain Perception for DEMO III," in *Proc. IEEE Intelligent Vehicles Symposium*, pp. 326-332, 2000.
- [27] D. Golda, K. Iagnemma, and S. Dubowsky, "Probabilistic Modeling and Analysis of High-Speed Rough-Terrain Mobile Robots," *Proceedings of the 2004 IEEE International Conference on Robotics and Automation*, 2004
- [28] D. Golda, *Modeling and Analysis of High-Speed Mobile Robots Operating on Rough Terrain*, M.S. Thesis, Massachusetts Institute of Technology, 2003.
- [29] T. Gillespie, *Fundamentals of Vehicle Dynamics*, Society of Automotive Engineers, 1992.
- [30] H. Pacejka, "The Tire as a Vehicle Component," *The XXVI FSITA Congress*, 1996.
- [31] R.A. Jarvis, "Distance Transform based Path Planning for Robot Navigation," In Y. F. Zheng, editor, *Recent Trends in Mobile Robots*, Ch. 1, pp. 3-31. World Scientific, Singapore, 1993.

- [32] Krishna, K., and Kalra, P., “Solving the Local Minima Problem for a Mobile Robot by Classification of Spatio-Temporal Sensory Sequences,” *Journal of Robotic Systems*, Vol. 17, No. 10, pp. 549-564, 2000.

Near-Optimal Navigation of High Speed Mobile Robots on Uneven Terrain

Karl Iagnemma, Shingo Shimoda, and Zvi Shiller

Abstract—This paper proposes a method for near-optimal navigation of high speed mobile robots on uneven terrain. The method relies on a layered control strategy. A high-level planning layer generates an optimal desired trajectory through uneven terrain. A low-level navigation layer guides a robot along the desired trajectory via a potential field-based control algorithm. The high-level planner is guaranteed to yield optimal trajectories but is computationally intensive. The low-level navigation layer is sub-optimal but computationally efficient. To guard against failures at the navigation layer, a model-based lookahead approach is employed that utilizes a reduced form of the optimal trajectory generation algorithm. Simulation results show that the proposed method can successfully navigate a mobile robot over uneven terrain while avoiding hazards. A comparison of the method's performance to a similar algorithm is also presented.

I. INTRODUCTION AND PREVIOUS WORK

UNMANNED ground vehicles (UGVs) are expected to play significant roles in future military, planetary exploration, and materials handling applications [1]. Many applications require UGVs to move at high speeds on rough, poorly characterized terrain. Ideally, UGVs would follow optimal (i.e. minimum time or maximum speed) trajectories during these operations to maximize efficiency, productivity, or other metrics.

Optimal performance is difficult to achieve in practice for several reasons. First, UGVs generally have access only to coarse-grained (i.e. several vehicle lengths spacing per data point) map data during the trajectory planning stage. Thus, while planned trajectories may be theoretically optimal at the data resolution available, they are likely to be sub-optimal, or even infeasible, at the data resolution relevant to the navigation task (i.e. several data points per vehicle length). Second, during high speed navigation, UGVs will likely encounter unexpected hazards that must be quickly (i.e. O(ms)) avoided. To avoid these hazards, navigation algorithms must be computationally efficient while considering important vehicle dynamic effects such as rollover and side slip.

Despite the wide interest in motion planning, few off-road trajectory planners have been developed [2]-[6]. Off-road trajectory planners cannot rely on a binary representation of

obstacles and free space, which is common to most work on motion planning. Instead, traversability over uneven terrain is determined not only by the size of obstacle, but also by terrain slope and curvature, and vehicle dynamics and speed. A kinematic planner was presented in [3] that computes the shortest feasible path for off-road vehicles. While the selected path is ensured to be statically safe, it does not account for vehicle dynamics and speed. A genetic algorithm is used in [4] to synthesize paths from segments, each evaluated for static stability and for satisfying mission constraints. Another genetic-based planner [6] uses fuzzy logic to account for obstacle height in each terrain region, which in turn determines vehicle speed. A similar approach to represent traversability is used in [7].

Off-road planners that explicitly consider vehicle dynamics typically search for an optimal path using dynamic simulations to determine the traversability or cost of specific terrain segments [5, 8]. An exception is the global trajectory planner first presented in [2]. It determines traversability directly by computing the maximum speed above which a vehicle will rollover or skid along a given terrain segment. The global search first selects a series of "best" traversable paths, which are then further optimized to minimize travel time. Early work derived speed limits for a simple point mass robot model [2]. Recent work considered more detailed vehicle models [9].

Artificial potential fields have long been successfully employed for robot navigation. First works were performed by Khatib as a real-time obstacle avoidance method for manipulators [10]. Ge et al. applied a potential field method for dynamic control of a mobile robot, with moving obstacles and goal [11]. Latombe applied potential field methods to general robot path planning [12]. Path planning using artificial potential fields has also been applied to nonholonomic systems [13]. Potential field navigation for wheeled robots on natural terrain has also been explored [14]. In general, potential field methods have been used for planning and control of low-speed systems, usually with a binary obstacle representation.

This paper presents a method for near-optimal navigation of high speed mobile robots on uneven terrain. The method relies on a layered control strategy. A high-level planning layer generates an optimal desired trajectory that is represented as a series of waypoints. The trajectory generation method is based on the global physics-based planner first presented in [2]. In the scenario considered here, this trajectory is formulated off-line based on coarse

Karl Iagnemma is with the Department of Mechanical Engineering, Massachusetts Institute of Technology, Cambridge MA, USA (e-mail: kdi@mit.edu). Shingo Shimoda is with the RIKEN BMC, JAPAN (e-mail: shimoda@bmc.riken.jp). Zvi Shiller is with the Department of Mechanical Engineering-Mechatronics, College of Judea and Samaria, Ariel, Israel (shiller@yosh.ac.il).

topographical map data, and thus computational constraints are minimal. A low-level navigation layer then guides the robot along the desired trajectory via a potential field-based control algorithm based on previous work by the authors [15]. In this method, a potential field is defined in the two-dimensional “trajectory space” of the robot path curvature and longitudinal velocity based on fine-grained elevation data gathered from on-board sensors [16]. Previous work required ad hoc tuning of potential field gains to yield safe robot navigation in practice. Here, to guard against failure a model-based lookahead approach is employed that utilizes a reduced form of the optimal trajectory generation algorithm. Simulation results show that the proposed method can successfully navigate a mobile robot over uneven terrain while avoiding hazards. A comparison of the method’s performance to a similar algorithm is also presented.

II. OPTIMAL TRAJECTORY PLANNING

Motion planning over rough terrain requires the selection of a feasible path, and the computation of some velocity profile along that path. If optimal performance is not required, the path can be generated first to ensure that the UGV is statically stable using a kinematic planner, such as in [3]. Then, the velocity profile along that path can be computed to ensure that the vehicle is also dynamically stable. While computationally efficient, such a path-velocity decomposition cannot yield the time optimal trajectory since the kinematic search is not guided by the vehicle’s dynamic performance. For this reason, the search for the optimal trajectory is normally done in the vehicle’s $2n$ dimensional state-space, for an n dimensional configuration space.

To avoid an expensive search in the state-space, the global trajectory optimization used here is formulated as a two stage optimization that combines a global “kinematic” graph search over the terrain with a local trajectory optimization [2]. The global search selects promising candidate paths for local optimization, thus trading an expensive search in the state-space for many simpler searches in the configuration space. A byproduct of this approach is the generation of local minima in addition to the global optimal trajectory [2, 17].

A. Terrain Representation

Terrain is here represented by a smooth bi-cubic B patch, which is a parametric surface made of a mesh of cubic splines. The need for a smooth surface representation stems from the local optimization, which requires a smooth path over the terrain surface.

Topologically, the patch is a warped rectangle in a three dimensional space. This terrain representation does not distinguish between obstacles and uneven terrain. Obstacles are simply integrated into the B-patch. The control points of the patch are generated by placing a uniform grid on the map-range data. The resolution of this grid depends on the map range. For short-range planning (up to 100 m), the resolution is chosen empirically at half the UGV width. This

ensures that obstacles the size of the vehicle and larger are depicted by the B-patch. For long range planning (up to several kilometers), the resolution is selected at 100 m between control points to account for primary terrain features (i.e. hills, ravines, etc.).

B. Velocity Limits

The global search produces path candidates for local trajectory optimization. Since we seek the time optimal trajectory, the global search selects paths along which the UGV can sustain high speeds without violating dynamic constraints such as rollover, excessive side slip, and maintaining ground contact. Velocity limits (above which some of the dynamic constraints may be violated) are computed by mapping the dynamic constraints to constraints on the vehicle’s speed and tangential acceleration. For long range planning, the UGV is modeled as a suspended point mass [2, 18]. For short range planning, the vehicle is modeled as a rigid body [9].

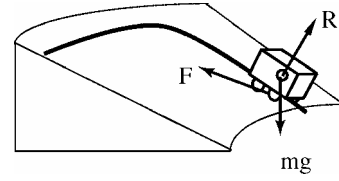


Fig. 1: External forces acting on a point mass UGV model.

Velocity limits for a point mass model are derived by first expressing the three external forces shown in Fig. 1 in terms of the UGV’s speed and tangential acceleration (see [2,18] for a detailed derivation):

$$\begin{aligned} f_t &= mgk_t + m\ddot{s} \\ f_q &= mgk_q + m\kappa n_q \dot{s}^2 \\ R &= mgk_r + m\kappa n_r \dot{s}^2 \end{aligned} \quad (1)$$

where f_t and f_q are components of the friction force tangent and normal to the path, κ is the path curvature, k is a unit vector pointing opposite of the gravity force, n is a unit vector pointing in the direction of the path center of curvature, and the subscripts denote projections along the path coordinate frame, t, q, r .

We can now express the dynamic constraints in terms of the external forces (1). The sliding constraint becomes:

$$f_t^2 + f_q^2 \leq \mu^2 R^2 \quad (2)$$

The tip-over constraint becomes:

$$f_q^2 \leq \left(R \frac{b}{h}\right)^2 \quad (3)$$

where h is the height of the center of mass and b is the lateral distance between the wheels. The contact constraint is simply:

$$R > 0 \quad (4)$$

Substituting (1) into the dynamic constraints (2-4) yields three constraints on vehicle speed. For example, the sliding constraint yields the following velocity constraint [18]:

$$a\dot{s}^4 + 2b\dot{s}^2 + c \geq 0 \quad (5)$$

where the coefficients a , b , c are determined from terrain geometry, path direction and curvature, and the terrain tractive coefficient. Staying below the speed limits obtained from the three dynamic constraints ensures that the vehicle does not roll, skid, or lose contact with the terrain.

C. The Global Search

The maximum velocity \dot{s}_m , above which the vehicle cannot follow the given path is an excellent candidate for measuring traversability since it accounts for the effects of vehicle dynamics, terrain topography, and surface friction. A zero value implies that the vehicle is statically unstable, and the given path segment is hence not traversable, whereas a nonzero value implies that the given path segment is traversable at some nonzero speed. The velocity limit thus offers a *scalar* function that can distinguish between traversable and non-traversable path segments in the configuration space.

Dividing the path arc length by the velocity limit produces a simple cost function that has units of time and can be computed for each path segment along the graph used to represent the terrain:

$$J = \int_{s_1}^{s_2} \frac{ds}{\dot{s}_m} \quad (6)$$

Note that (6) resembles the cost function used to minimize time except that here the actual vehicle speed \dot{s} is replaced with the speed limit \dot{s}_m . Thus, using cost function (6) produces the fastest traversable paths, assuming that the vehicle travels at its maximum safe speed. The ability to select a traversable path at high speeds without the need for an expensive search in the state-space greatly contributes to the efficiency of this approach.

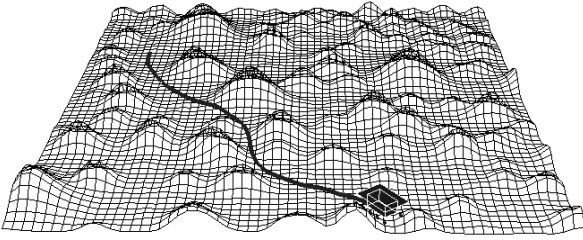


Fig. 2: A global optimal path over rough terrain.

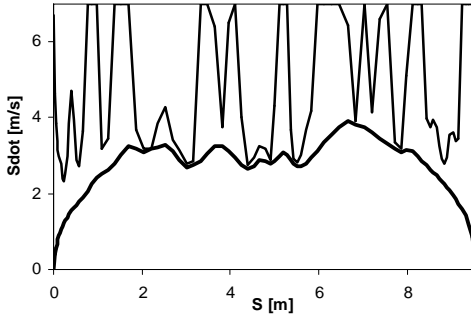


Fig. 3: An optimal velocity profile along the path in Fig. 2. The velocity profile stays below the velocity limits.

The global search first generates a series of “best” traversable paths. These paths are good initial guesses for a local trajectory optimization that will minimize motion time and take into account the feasible vehicle acceleration along the path (ignored during the global grid search). The local optimization consists of a parameter optimization over the control points of a B spline that define the path over the B-patch. The end result of this two stage process is a globally optimal trajectory that minimizes motion time from start to goal, while considering vehicle dynamics, terrain topography, and the vehicle’s dynamic constraints. Figs. 2 and 3 show an optimal path and optimal velocity profile computed by the global search between given end points on uneven terrain. The optimal velocity profile, shown in Fig. 3, is computed by switching between the maximum and minimum tangential acceleration to avoid crossing the velocity limit curve. Obviously, the optimal velocity profile represents the ultimate vehicle speeds along the path since any attempt to move faster would cross the velocity limits, which in turn would cause the vehicle to either roll, skid, or lose contact with the terrain.

III. TRAJECTORY SPACE NAVIGATION WITH POTENTIAL FIELDS

Here, a potential field-based navigation method is employed as the low-level navigation layer. It takes as an input an optimal trajectory (computed as described in Section II) represented as a list of closely-spaced waypoints. A more thorough presentation can be found in [15].

The trajectory space, $TS \in \mathbb{R}^2$, is defined as a two-dimensional space of a UGV’s instantaneous path curvature and longitudinal velocity [16]. This space clearly cannot describe the complete vehicle state, but can rather capture important UGV state and configuration information and serve as a physically intuitive description of the current vehicle status. A UGV’s “position” in TS is a curvature-velocity pair denoted $\tau = (v, k)$. Note that in this work only positive longitudinal velocities are considered.

The trajectory space is a convenient space for navigation for two reasons. First, the trajectory space maps easily to the UGV actuation space (generally consisting of the throttle and steering angle). Navigation algorithms performed in the trajectory space will select command inputs that obey vehicle nonholonomic constraints. Second, dynamic constraints related to UGV rollover and side slip are easily expressible in the trajectory space, since these constraints are functions of the UGV velocity and path curvature. These constraints can also capture effects such as terrain inclination and roughness.

The coordinate systems used in this work are shown in Fig. 4. A body frame \mathcal{B} is fixed to the vehicle, with its origin at the vehicle center of mass. The position of the vehicle in the inertial frame \mathcal{I} is expressed as the position of the origin of \mathcal{B} . The vehicle attitude is expressed by x - y - z Euler angles using the vehicle yaw θ , roll ϕ , and pitch ψ defined in \mathcal{B} .

To perform navigation a potential field is constructed in the trajectory space based on dynamic constraints, waypoint

locations, and hazard locations. These issues are discussed below.

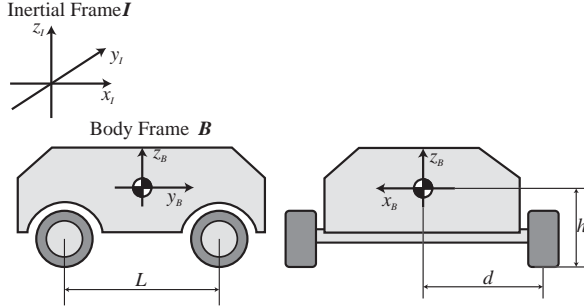


Fig. 4. Definition of coordinate system.

A. Potential Field Constraint Definitions

Potential fields are defined based on UGV rollover and side slip constraints. As in the high-level planning layer, these constraints are computed from rigid body models. A rollover constraint for a UGV on uneven terrain can be expressed as:

$$\kappa_r(v) = \frac{dg_z \pm hg_x}{hv^2} \quad (7)$$

where κ_r is the maximum admissible path curvature and g_* is the gravitational acceleration of the z -axis direction in **B**. The two solutions to (7) correspond to travel on positive/negative inclination slopes with nonzero g_x components reflecting the effect of terrain roll. A potential field is then defined as:

$$PF_r(v, \kappa) = \begin{cases} K_r \left(1 - \left(\frac{(\kappa - \kappa_{MAX})^2}{(\kappa_r(v) - \kappa_{MAX})^2} \right) \right) & \kappa_r \leq \kappa < \kappa_{MAX} \\ 0 & 0 \leq \kappa < \kappa_r \end{cases} \quad (8)$$

where κ_{MAX} is the maximum attainable path curvature based on kinematic steering constraints, and K_r is a positive gain parameter to modulate the potential field amplitude.

A side slip constraint for a UGV on uneven terrain can be expressed as:

$$\kappa_s(v) = \frac{-g_x \pm \mu g_z}{v^2} \quad (9)$$

where κ_s is the maximum admissible path curvature and μ is the terrain tractive coefficient. A potential field is then defined as:

$$PF_s(v, \kappa) = \begin{cases} K_s \left(1 - \left(\frac{(\kappa - \kappa_{MAX})^2}{(\kappa_s(v) - \kappa_{MAX})^2} \right) \right) & \kappa_s \leq \kappa < \kappa_{MAX} \\ 0 & 0 \leq \kappa < \kappa_s \end{cases} \quad (10)$$

Again, K_s is a positive gain parameter to modulate the potential field amplitude.

B. Potential Field-Based Waypoint Navigation

For navigation between waypoints, a desired path curvature and velocity must be computed at each instant based (at minimum) on the relative location of the robot and the waypoint. A method for computing a path curvature based on knowledge of UGV steering kinematics and waypoint position is presented in [15]. A potential field corresponding to the current desired waypoint location can then be defined as follows:

$$PF_g(\kappa) = K_g(\kappa - \kappa_d)^2 \quad (11)$$

where κ_d is the desired steering angle and K_g is a positive gain parameter to modulate the potential field amplitude.

C. Potential Field for Desired Velocity

A potential field for the desired UGV velocity can be simply expressed as follows:

$$PF_v(v) = K_{v1}(v - v_d)^{K_{v2}} \quad (12)$$

where v_d is the desired velocity and K_{v1} and K_{v2} are positive gain parameters to modulate the potential field amplitude. v_d can be a function of position to reflect mission objectives.

D. Potential Field for Hazard Locations

Consider a UGV approaching a hazard as shown in Fig. 5. Here κ_1 and κ_2 are the maximum and minimum path curvatures that intersect the hazard. A potential field for hazard locations is constructed based on the following observations:

- Path curvatures between κ_1 and κ_2 can be safely followed until the UGV is near the hazard;
- The potential field magnitude should be greater at high speed than at low speed since control accuracy generally decreases with increasing speed;
- Relative locations of waypoints and hazards should influence the hazard potential field value (i.e. to allow close passage to hazards to achieve a waypoint).

From these observations, a potential field for hazard locations is defined as follows:

$$PF_o(v, \kappa) = \frac{K_o(K_{ov}v + 1)}{(K_{od}O_d + 1)(K_{oa}A_d + 1)} \exp\left(-\frac{(\kappa - X)^2}{2\sigma}\right) \quad (13)$$

where O_d is the Euclidean distance between vehicle and hazard, A_d is the angle between the UGV heading and the waypoint location, $X = (\kappa_1 + \kappa_2)/2$, $\sigma = (\kappa_1 - \kappa_2)/2$, and K_o , K_{od} , K_{oa} , and K_{ov} are positive gain parameters to modulate the potential field amplitude.

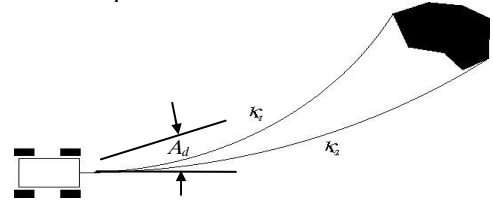


Fig. 5. Minimum and maximum path curvatures intersecting with a hazard.

E. Definition of Net Potential Field

A net potential field is generated as the sum of all proposed potential fields, as follows:

$$PF(v, \kappa) = PF_r(v, \kappa) + PF_s(v, \kappa) + PF_g(\kappa) + PF_v(v) + \sum_{i=1}^n PF_o^i(v, \kappa) \quad (14)$$

where n is the number of hazards present and PF_o^i is the potential function corresponding to the i^{th} hazard. An illustration of a net potential field is shown in Fig. 6.

At every timestep, a desired path curvature and velocity are determined by calculating the gradient of the net potential field at the robot position in TS , then moving in the direction of maximum descent. Details related to these computations

and issues related to potential field local minima and maxima are described in [15].

The potential field navigation method described here has been shown to perform well in simulation and experiments. However, studies have shown that terrain with high-frequency undulation can potentially lead to rollover and side slip failures. This is due to the fact that the potential field constraints related to rollover and side slip are computed as a function of the average local terrain inclination. Thus, large localized values of inclination can lead to failure.

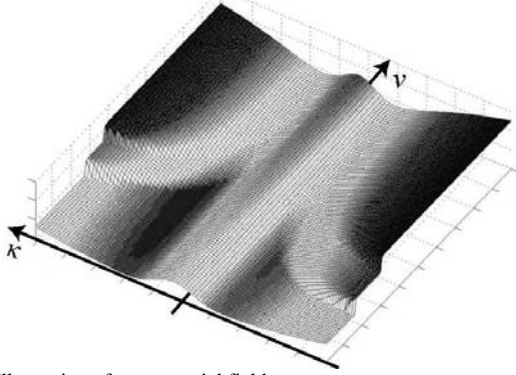


Fig. 6. Illustration of net potential field.

To guard against failures at the navigation layer, a model-based lookahead approach has been developed that utilizes a reduced form of an optimal trajectory generation algorithm. This approach is described next.

IV. NEAR-OPTIMAL POTENTIAL FIELD NAVIGATION

A common weakness of potential field methods is that it is difficult to guarantee convergence and bound system performance. While the potential field-based navigation method described here has been shown to perform effectively in simulation and experimental studies, the authors have observed failures in cases where significant high-frequency terrain undulation exists. This is due to the fact that potential functions related to rollover and side slip constraints are computed as a function of the average local terrain inclination. Thus, large localized values of inclination can lead to failure.

To guard against failure at the navigation layer a model-based lookahead approach is employed that utilizes a reduced form of the optimal trajectory generation algorithm. At every timestep, this approach essentially forward simulates a robot model over a short time horizon, then determines whether the robot will violate any dynamic constraints along the resulting trajectory. Violation of dynamic constraints is determined by comparing the robot's predicted velocity profile to the maximum safe allowable velocity profile computed via the method described in Section II. If a constraint is violated, the robot's desired velocity is reduced to the maximum safe velocity along the trajectory. This has the effect of imposing a "safe speed limit" on the robot at the navigation layer.

The algorithm for calculating a safe robot maneuver at every timestep is described here, with T representing the time horizon duration and t the "virtual time" in a forward

simulation loop. The value of T is here chosen empirically. The algorithm is composed of the following steps:

1. The value of the net potential field at the robot's current position in TS is calculated from Eqn. (14);
2. The gradient of the net potential field is computed, and a desired maneuver (i.e. a (v, κ) pair) is chosen in the direction of maximum descent;
3. The predicted trajectory of the robot is computed via forward simulation of a rigid body model subject to the desired maneuver over time dt ;
4. Steps 1-3 are repeated while $t < T$;
5. A maximum safe velocity profile is computed over the predicted path via the approach described in Section II;
6. The predicted robot velocity profile is compared to the maximum safe velocity profile. If the predicted velocity profile exceeds the maximum safe velocity profile at any point, the robot's desired velocity is reduced to the maximum safe velocity along the trajectory.

This approach attempts to exploit the computational efficiency of the potential field-based navigation with the safety guarantees implicit in optimal trajectory planning. Since low-order rigid body models are used in forward simulation, computational demands are negligible.

V. SIMULATION RESULTS

Dynamic simulations were conducted of a small UGV traveling at high speeds over uneven terrain. The UGV parameters were as follows (see Fig. 4): length $L = 0.27$ m, half-width $d = 0.124$ m, c.g. height $h = 0.06$ m, wheel diameter $= 0.12$ m. The potential field parameters were set as follows: $K_r = 800$, $K_s = 800$, $K_g = 0.3$, $K_{v1} = 0.5 \times 10^{-5}$, $K_{v2} = 4$, $K_o = 1500$, $K_{od} = 0.05$, $K_{oa} = 10$, $K_{ov} = 0.07$, $T = 1.0$ s.

Randomized rough terrain was generated using a fractal method modified to incorporate gross terrain undulation and discrete "peaks." Rough terrain with fractal number of 2.05, grid spacing of 2 wheel diameters, and height scaling of 35 wheel diameters was employed. The near-optimal navigation method described above was used to determine the desired UGV steering angle and velocity. PD control was employed for steering angle and velocity control.

A representative simulation result is shown in Figs. 7-9. Fig. 7 shows a representative terrain, the optimal waypoints generated by the high-level planner, and the actual path followed by the low-level navigation layer. It can be seen that the UGV successfully navigates through the desired waypoints, thus approximating an optimal path while avoiding hazards. Fig. 8 shows a plot of the UGV velocity along the path compared to the maximum achievable velocity as computed by the model-based lookahead algorithm. The actual velocity remains near to the optimal velocity, and deviates from the desired velocity during hazard avoidance maneuvers and turns with large curvature. Fig. 9 shows plots of the UGV roll angle and slip angle during the simulation, illustrating the challenging nature of the terrain and effectiveness of the algorithm in limiting these quantities.

Table 1 shows the results of 25 simulation trials. The proposed near-optimal navigation method safely controlled

the UGV in all terrains. The average percent difference in total navigation time between the optimal method and the proposed method was 9.6%. It was observed that the “standard” potential-field based navigation scheme (i.e. without lookahead analysis) failed on 24% of the simulation trials, with a 23.6% average slower navigation time than the optimal traveling time. It should be noted that safer navigation with the “standard” approach is achievable, however at the expense of greater increase in navigation time.

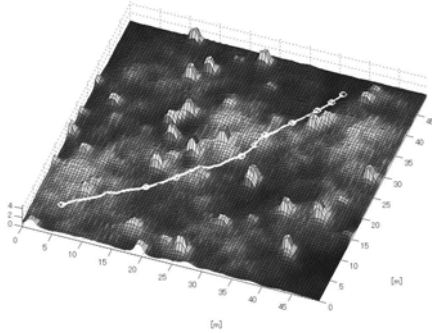


Fig. 7. Representative terrain map and waypoints generated by high-level planning layer and path generated by low-level navigation layer.

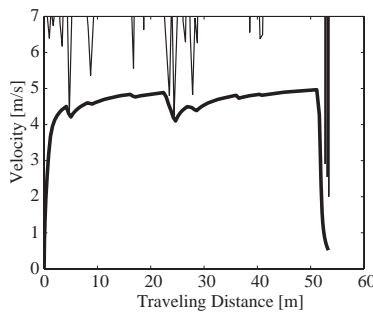


Fig. 8. UGV velocity (thick) and computed velocity limit curve (thin).

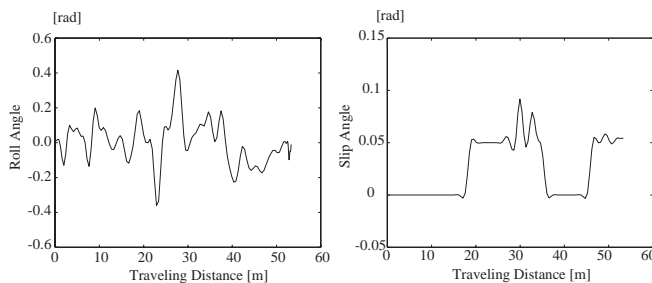


Fig. 9. UGV Roll angle (left) and slip angle (right).

TABLE I
SIMULATION RESULTS OF 25 TERRAIN TRAVERSALS

	Incidence of Failure [%]	Increase over Optimal Time [%]
Near-optimal	0.0	9.6
“Standard” Potential-field	24.0	23.6

VI. CONCLUSIONS

This paper proposes a method for near-optimal navigation of high speed mobile robots on uneven terrain. A high-level planning layer generates an optimal desired trajectory, and a low-level navigation layer guides a robot along the desired trajectory via a potential field-based algorithm. To guard against failures at the navigation layer, a model-based

lookahead approach was presented that utilizes a reduced form of the optimal trajectory generation algorithm. Simulation trials show that the proposed method can safely navigate a mobile robot along a near-optimal trajectory over uneven terrain while avoiding hazards.

ACKNOWLEDGMENTS

K. Iagnemma acknowledges the support of the U.S. Army Research Office grant number W911NF-05-1-0166. Z. Shiller acknowledges the support of the Israeli Space Agency grant 01-99-08430 and the support of Dr. David Paslin for the Robotics Research Laboratory at the College of Judea and Samaria.

REFERENCES

- [1] S. Fish, “UGV’s in Future Combat Systems,” *Proceedings of SPIE - The International Society for Optical Engineering*, v 5422, *Unmanned Ground Vehicle Technology VI*, pp. 288-291, Apr 2004.
- [2] Z., Shiller and Y.R., Gwo, “Dynamic motion planning of autonomous vehicles,” *IEEE Transactions on Robotics and Automation*, 7(2):241-249, April 1991.
- [3] T. Simeon and B. Dacre-Wright, “A practical motion planner for all-terrain mobile robots,” *International Conference on Intelligent Robots and Systems*, pp. 1357-1363, 1993.
- [4] S. Farritor, H. Hacot and S. Dubowsky, “Physics-based planning for planetary exploration,” *Proceedings of the IEEE Int. Conf. on Robotics and Automation*, 1998.
- [5] M. Cherif, “Motion Planning for All-Terrain Vehicles: A Physical Modeling Approach for Coping with Dynamic and Contact Interaction Constraints,” *IEEE Transactions on Robotics and Automation*, vol. 15, no. 2, pages 202-218, April 1999.
- [6] M. Tarokh, R. Chan and C. Song, “Path planning of rovers using fuzzy logic and genetic algorithm,” *Proc. World Automation Conf., ISORA-026*, pp. 1-7, 2000.
- [7] H. Seraji, “Traversability index: A new concept for planetary rovers,” *Proceedings of IEEE Int’l. Conf. on Robotics and Automation*, 1999.
- [8] A. Kelly and A. Stentz, “An Approach to Rough Terrain Autonomous Mobility,” *International Conference on Mobile Planetary Robots*, 1997.
- [9] M. P. Mann and Z. Shiller, “Dynamic Stability of Off-Road Vehicles: A Geometric Approach,” *Proceedings of IEEE Int. Conf. on Robotics and Automation*, pp. 3705-3710, 2006.
- [10] O. Khatib, “Real-time Obstacle Avoidance for Manipulators and Mobile Robots,” *International Journal of Robotics Research*, Vol. 5, No. 1, pp. 90-98, 1986.
- [11] S. Ge and Y. Cui, “Dynamic Motion Planning for Mobile Robots Using Potential Field Method,” *Autonomous Robots*, Vol. 13, 2002.
- [12] J. Barraquand and B. Langlois and J. Latombe, “Numerical Potential Field Techniques for Robot Path Planning,” *IEEE Trans. on Systems, Man, and Cybernetics*, Vol. 22, No.2, pp. 224-241, 1992.
- [13] H. Tanner, S. Loizou, and K. Kyriakopoulos, “Nonholonomic Navigation and Control of Cooperating Mobile Manipulators,” *IEEE Transaction on Robotics and Automation*, Vol. 19, No. 1, 2003.
- [14] H. Haddad, M. Khatib, S. Lacroix and R. Chatila., “Reactive Navigation in Outdoor Environments using Potential Fields,” *Proc. of Intl. Conf. on Robotics and Automation*, pp. 1232-1237, 1998.
- [15] Shimoda, S., Kuroda, Y., and Iagnemma, K., “High Speed Navigation of Unmanned Ground Vehicles on Uneven Terrain using Potential Fields,” to appear in *Robotica*, 2007.
- [16] Spenko, M., Kuroda, Y., Dubowsky, S., and Iagnemma, K., “Hazard Avoidance for High Speed Unmanned Ground Vehicles in Rough Terrain,” *Journal of Field Robotics*, Vol. 23, No. 5, pp. 311-331, 2006.
- [17] Shiller, Z., Fujita, Y., Ophir, D., Nakamura, Y., “Computing a set of Local Optimal Paths through Cluttered Environments and Over Open Terrain,” *IEEE Int. Conf. on Robotics and Automation*, 2004.
- [18] Z., Shiller, “Obstacle Traversal for Space Exploration,” *Proceedings of the IEEE Int. Conf. on Robotics and Automation*, 2000.

Analysis, Design, and Control of an Omnidirectional Mobile Robot in Rough Terrain

Martin Udengaard and Karl Iagnemma

Department of Mechanical Engineering
Massachusetts Institute of Technology
77 Massachusetts Ave. Cambridge, MA 02139
{mru, kdi} @ mit.edu

An omnidirectional mobile robot is able, kinematically, to move in any direction regardless of current pose. To date, nearly all designs and analyses of omnidirectional mobile robots have considered the case of motion on flat, smooth terrain. In this paper, an investigation of the design and control of an omnidirectional mobile robot for use in rough terrain is presented. Kinematic and geometric properties of the active split offset caster drive mechanism are investigated along with system and subsystem design guidelines. An optimization method is implemented to explore the design space. Use of this method results in a robot that has higher mobility than a robot designed using engineering judgment. A simple kinematic controller that considers the effects of terrain unevenness via an estimate of the wheel-terrain contact angles is also presented. It is shown in simulation that under the proposed control method, near-omnidirectional tracking performance is possible even in rough, uneven terrain.

1 Introduction

Mobile robots are finding increasing use in military [1], disaster recovery [2], and exploration applications [3]. These applications frequently require operation in rough, unstructured terrain. Currently, most mobile robots designed for these applications are tracked or Ackermann-steered wheeled vehicles. Methods for controlling these types of robots in both smooth and rough terrain have been well studied [4-6]. While these robots can perform well in many scenarios, navigation in cluttered, rocky, or obstacle-dense urban environments can be difficult or impossible. This is partly due to the fact that traditional tracked and wheeled robots must reorient to perform some maneuvers, such as lateral displacement. Omnidirectional mobile robots could potentially navigate faster and more robustly through cluttered urban environments and over rough terrain, due to their ability to track non-smooth motion profiles.

An omnidirectional mobile robot is able, kinematically, to move in any direction regardless of current pose. Previous researchers have proposed and developed omnidirectional mobile robots employing a wide variety of wheel types including roller [7, 8], Mecanum [9, 10], and spherical wheels [11, 12].

Roller wheel designs, as shown in Fig. 1, employ small rollers along the outer edge of a “primary” wheel to allow traction in the wheel’s longitudinal direction and free rolling in the lateral direction. Omnidirectional motion is obtained by orienting several of these wheels in different directions. These wheels are inexpensive, easy to control, and operate well in flat, indoor environments.



Figure 1. An example of a sliding wheel (from [8]).

Mecanum wheels are similar to roller wheels in that they employ rollers along the outer edge of a wheel; however the rollers are aligned at an angle to produce angular contact forces with the ground. Robots equipped with four Mecanum wheels, as shown in Fig. 2, can produce omnidirectional motion (see Fig. 3). Again, these wheel types have proved to be simple to control and effective on flat, indoor terrain.

Roller and Mecanum wheels are unsuitable for outdoor environments, where debris can clog the rollers and alter the friction characteristics of the wheels [13]. Also, the (relatively) small rollers on the edge of each primary wheel can be subjected to significant loads, which can lead to high ground pressure and large sinkage in deformable outdoor terrain.

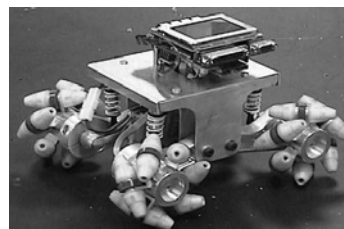


Figure 2. An example of a robot using four Mecanum wheels (from [9]).

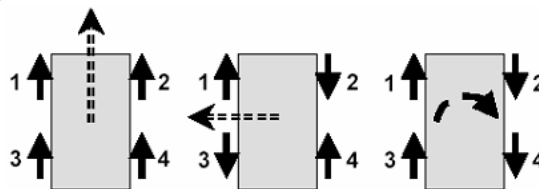


Figure 3. A schematic showing the omnidirectional capabilities of a Mecanum wheel driven omnidirectional robot (from [9]). The solid arrows indicate the driven direction of each wheel, and the dashed arrows indicate translation and rotation of the robot.

Spherical wheel designs, as shown in Fig. 4, employ frictional drive rollers to allow rolling in any direction. Since the drive rollers rely on friction to transmit energy to the wheel, debris could potentially foul the transmission mechanism in rough, outdoor environments. Due to the two dimensional curvature of the sphere, the contact patch is smaller than that of a traditional wheel, leading to increased ground pressure given the same ground reaction force.

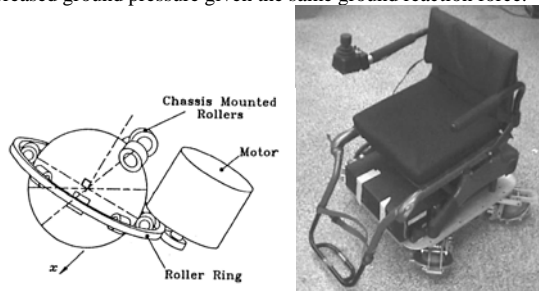


Figure 4. A schematic showing a spherical wheel (left) and its use on an omnidirectional wheelchair (right) (from [12]).

Near-omnidirectional motion has been achieved using steerable wheels [14]. As shown in Fig. 5, these designs have a wheel mounted to an orthogonal steering actuator. The steering actuator can rotate the wheel to orient it in any planar direction. These wheels can employ standard tires, and have proven effective in outdoor environments. However they are not truly omnidirectional (i.e. the

resulting vehicle kinematics are subject to nonholonomic constraints) since they must undergo wheel slip and/or scrubbing to change direction. This can result in deteriorated path tracking and substantial energy loss. Note that similar designs based on offset caster wheels do allow omnidirectional motion with standard tires [15]. Analysis of this design has been studied extensively for operation on flat ground.

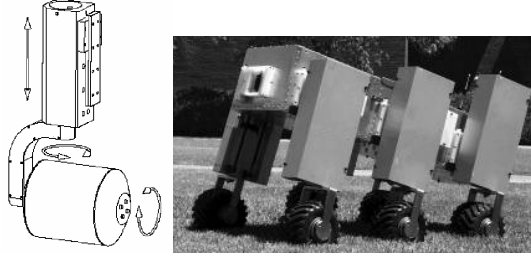


Figure 5. A schematic showing a steerable wheel (left) and its use on an outdoor mobile robot (right) (from [14]).

An omnidirectional mobile robot driven by active split offset casters (ASOCs) was initially proposed in [16] for use in structured, indoor environments. ASOC drives employ conventional wheel designs that do not rely on frictional contact, and are thus potentially suitable for use in dirty, outdoor environments. They also can be designed with little constraint on wheel diameter and width, and thus can potentially tolerate large loads with low ground pressure. Finally, ASOC modules can be integrated with suspension systems that allow for traversal of uneven terrain [17]. Therefore ASOC-driven omnidirectional mobile robots hold promise for use in rough, unstructured environments.

In this paper, an investigation of the design and control of an ASOC-driven omnidirectional mobile robot for use in rough terrain is presented. This paper is organized as follows: in Section 2, kinematic and geometric properties of the drive mechanism are analyzed, in Section 3, guidelines for robot design are presented and an optimization method is implemented to explore the design space, and in Section 4, a simple kinematic controller that considers the effects of terrain unevenness via an estimate of the wheel-terrain contact angles is presented. These analyses can be used as design guidelines for development of an omnidirectional mobile robot that can operate in unstructured environments. The optimization method is shown to generate design parameters for a robot that has higher mobility than a robot designed using engineering judgment. It is shown in simulation that under the proposed control method, near-omnidirectional tracking performance is possible even in rough, uneven terrain.

2 The Active Split Offset Caster

Active split offset caster (ASOC) drive modules possess the ability to achieve omnidirectional motion via a driven wheel pair. Figure 6 shows the ASOC module considered in this study. The assembly consists of a split wheel pair, a connecting axle, and an offset link connecting the wheel pair to the mobile robot body. Each wheel is independently driven about the axis θ . The axle connecting the wheel pair can pivot about the axis β . The axle pivot can be passive or active, and allows the wheel pair to adapt to terrain unevenness, therefore increasing the likelihood of continuous terrain contact for each wheel even during travel on rough terrain. The wheel pair/axle assembly rotates about axis α . As with the axle pivot, the assembly rotation axis can also be active or passive. This axis connects the ASOC module to a robot body or a passive or active suspension element. L_{offset} is the distance between the axis α and the axis θ . L_{split} is the distance between the wheels.

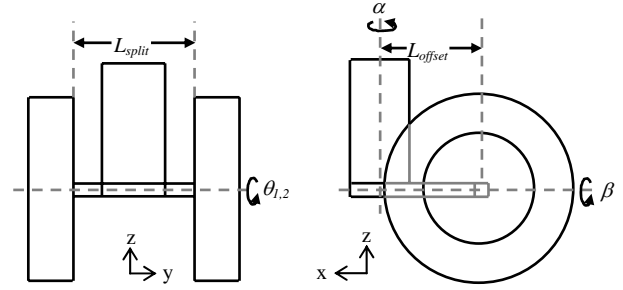


Figure 6. Active split offset caster wheel assembly front view (left) and side view (right).

By independently controlling each wheel's velocity, an ASOC module can produce arbitrary (planar) translational velocities at a point along its α axis [16]. Two or more ASOCs attached to a rigid robot body can thus produce arbitrary translational and rotational robot velocities. Therefore, an ASOC-driven omnidirectional robot must minimally employ two ASOC modules, and can employ more to meet other design requirements related to thrust, ground pressure, tip-over stability, etc. Note that passive or active casters can also be used to augment ASOC modules to meet these requirements.

2.1 Isotropy Analysis

Path following in rough terrain may require a robot to quickly change its direction of travel. All holonomic omnidirectional mobile robots are kinematically able to instantaneously move in any planar direction. However, while some omnidirectional mobile robots exhibit preferred directions of travel, others exhibit equal mobility characteristics in all directions. Such robots are said to exhibit "isotropic mobility." Hence, isotropy is used to quantify the system's omnidirectional mobility.

Kinematic isotropy is defined as the condition in which a robot possesses a constant input velocity/output velocity ratio for all possible output velocity directions [15]. An isotropy metric is a measure of how near a robot is to the isotropy condition, and increases from 0.0 for a singular configuration (i.e. purely anisotropic, or non-omnidirectional) to 1.0 for kinematic isotropy. Ideally, an omnidirectional mobile robot should possess a metric value of 1.0 for all joint space configurations, and thus not exhibit a preferred direction of travel. This simplifies path planning and navigation by eliminating the effect of robot orientation on movement capability. The output directions considered in this study are two planar translations in the robot body frame, and rotation about the robot body frame z axis.

The isotropy metric for a given robot configuration can be computed as the ratio of the smallest to largest eigenvalues of the Jacobian matrix relating the driving module velocities to the robot body velocities [15]. The isotropy metric can be averaged over the entire configuration space (in this case, the rotation angles between each ASOC and the body, α) to yield an average measure of performance that could be used to compare candidate omnidirectional mobile robot designs.

2.2 Effect of ASOC Geometric Parameters on Isotropy

To analyze the effects of ASOC module kinematic parameters on isotropy, variations in the wheel radius, L_{offset} , and L_{split} were analyzed over a range of values that represent a practical omnidirectional robot design space. The Jacobian from wheel rotational velocities to α axis translational velocities in the ASOC frame is:

$$\begin{bmatrix} v_{long} \\ v_{lat} \end{bmatrix} = \begin{bmatrix} \frac{R_{wheel}}{2} & \frac{R_{wheel}}{2} \\ \frac{R_{wheel} \cdot L_{offset}}{L_{split}} & -\frac{R_{wheel} \cdot L_{offset}}{L_{split}} \end{bmatrix} \begin{bmatrix} \dot{\theta}_1 \\ \dot{\theta}_2 \end{bmatrix} \quad (1)$$

where v_{long} and v_{lat} are the longitudinal (x) and lateral (y) ASOC axis translational velocities, respectively (see Fig. 6). The wheel radius appears in each term exactly once, and cancels out when the ratios of

the eigenvalues are computed, thus the module isotropy is independent of the wheel radius.

In Fig. 7, a plot of isotropy is shown as a function of L_{offset} and L_{split} . An iso-height exists at an isotropy value of 1.0. This iso-height occurs at $L_{split} / L_{offset} = 2.0$. The sensitivity of isotropy to perturbations in L_{split} and L_{offset} is relatively high; a 10% change in L_{split} or L_{offset} decreases the isotropy metric value by up to 45% for small ASOC module sizes.

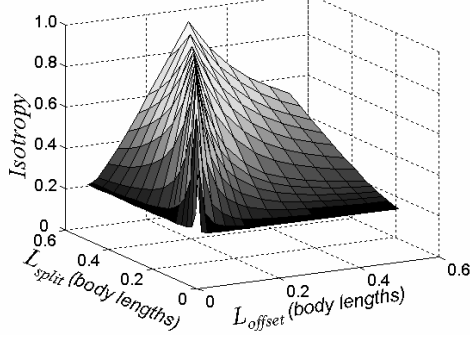


Figure 7. Mean isotropy for a four ASOC omnidirectional robot.

In Fig. 8, a plot of isotropy values over a range of L_{split} / L_{offset} ratios can be seen. There exists a single isotropy value for each L_{split} / L_{offset} ratio, indicating that isotropy is not an independent function of both L_{split} and L_{offset} . This is a useful insight for omnidirectional robot design. This also explains the sensitivity of isotropy to changes in L_{split} and L_{offset} for small ASOC modules sizes, since a unit change in L_{split} or L_{offset} results in a relatively large change in L_{split} / L_{offset} for small parameter values. As shown in equation (1), L_{split} and L_{offset} only appear as a ratio, and the Jacobian becomes isotropic (i.e. all eigenvalues are equal) when the ratio of L_{split} to L_{offset} is equal to 2.0.

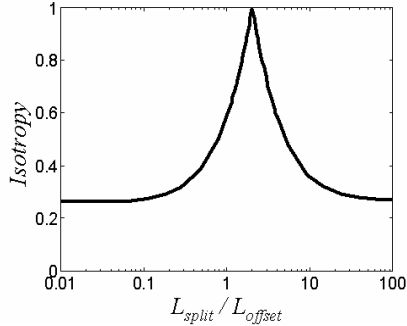


Figure 8. Average isotropy for an omnidirectional mobile robot driven by three ASOC modules as a function of L_{split} / L_{offset} .

2.3 Effect of ASOC Module Location on Isotropy

The relative location of ASOC modules with respect to one another also affects isotropy. A vehicle with three modules, shown in Fig. 9, was chosen for analysis. A plot of isotropy as a function of relative ASOC angular location is presented in Fig. 10. Each ASOC had an L_{split} / L_{offset} ratio of 2.0. ASOC physical interference was neglected.

The Jacobian of a three ASOC omnidirectional mobile robot is shown in (2). Analysis shows that maximum isotropy values (1.0) are obtained when the ASOC modules are evenly spaced and $L_{split} / L_{offset} = 2.0$. The value drops to 0 for the degenerate case where all ASOC modules coincide. A similar phenomenon is observed for robots with any number of ASOC modules. Thus to maximize isotropy, ASOC modules should be equally spaced.

$$J' = \frac{1}{3} \begin{bmatrix} \frac{\cos(\alpha_1) - L_{offset} \sin(\alpha_1)}{2 L_{split}} & \frac{\sin(\alpha_1) + L_{offset} \cos(\alpha_1)}{2 L_{split}} & \dots \\ \frac{\cos(\alpha_1) + L_{offset} \sin(\alpha_1)}{2 L_{split}} & \frac{\sin(\alpha_1) - L_{offset} \cos(\alpha_1)}{2 L_{split}} & \dots \\ \frac{\cos(\alpha_2) - L_{offset} \sin(\alpha_2)}{2 L_{split}} & \frac{\sin(\alpha_2) + L_{offset} \cos(\alpha_2)}{2 L_{split}} & \dots \\ \frac{\cos(\alpha_2) + L_{offset} \sin(\alpha_2)}{2 L_{split}} & \frac{\sin(\alpha_2) - L_{offset} \cos(\alpha_2)}{2 L_{split}} & \dots \\ \frac{\cos(\alpha_3) - L_{offset} \sin(\alpha_3)}{2 L_{split}} & \frac{\sin(\alpha_3) + L_{offset} \cos(\alpha_3)}{2 L_{split}} & \dots \\ \frac{\cos(\alpha_3) + L_{offset} \sin(\alpha_3)}{2 L_{split}} & \frac{\sin(\alpha_3) - L_{offset} \cos(\alpha_3)}{2 L_{split}} & \dots \end{bmatrix}$$

$$\begin{bmatrix} \frac{\sin(\alpha_1) + L_{offset} \cos(\alpha_1)}{2 L_{split}} \\ \frac{\sin(\alpha_1) - L_{offset} \cos(\alpha_1)}{2 L_{split}} \\ \cos(\gamma_1) \left(\frac{\sin(\alpha_2) + L_{offset} \cos(\alpha_2)}{2 L_{split}} \right) - \sin(\gamma_1) \left(\frac{\cos(\alpha_2) - L_{offset} \sin(\alpha_2)}{2 L_{split}} \right) \\ \cos(\gamma_1) \left(\frac{\sin(\alpha_2) - L_{offset} \cos(\alpha_2)}{2 L_{split}} \right) - \sin(\gamma_1) \left(\frac{\cos(\alpha_2) + L_{offset} \sin(\alpha_2)}{2 L_{split}} \right) \\ \cos(\gamma_2) \left(\frac{\sin(\alpha_3) + L_{offset} \cos(\alpha_3)}{2 L_{split}} \right) - \sin(\gamma_2) \left(\frac{\cos(\alpha_3) - L_{offset} \sin(\alpha_3)}{2 L_{split}} \right) \\ \cos(\gamma_2) \left(\frac{\sin(\alpha_3) - L_{offset} \cos(\alpha_3)}{2 L_{split}} \right) - \sin(\gamma_2) \left(\frac{\cos(\alpha_3) + L_{offset} \sin(\alpha_3)}{2 L_{split}} \right) \end{bmatrix} \quad (2)$$

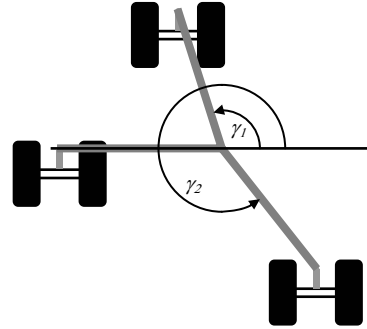


Figure 9. Top view of representative vehicle for ASOC location analysis.

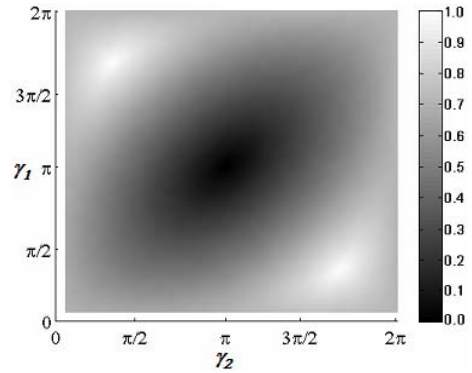


Figure 10. Isotropy as a function of ASOC module relative location.

2.4 Effect of Loss of Wheel Contact on Isotropy

When traversing rough terrain, loss of contact may occur between the wheels and the ground. In this case, system mobility will be decreased. An analysis of the isotropy of robots without full ground contact is presented in Table I. For comparison, robots with two, three, and four ASOC modules are examined. Each ASOC is allowed to possess full, partial (i.e. one wheel on the ground), or no ground contact. It is assumed that the ASOC modules are equally spaced and have $L_{split} / L_{offset} = 2.0$.

Table I Effect of Loss of Wheel Contact on Isotropy

Total # ASOCs	# no contact ASOCs	# partial contact ASOCs				
		0	1	2	3	4
2	0	1.000	0.464	0.000	N/A	N/A
3	0	1.000	0.706	0.504	0.270	N/A
	1	0.577	0.367	0.000	N/A	N/A
4	0	1.000	0.791	0.656	0.544	0.399
	1	0.707	0.574	0.482	0.259	N/A
	2	0.414	0.265	0.000	N/A	N/A

As expected, loss of wheel contact causes reduced isotropy due to a loss of full controllability of the ASOC modules. It can be observed that a four ASOC robot with one module that has completely lost terrain contact does not perform as well as a three ASOC vehicle in full contact. This is due to the fact that the three ASOC robot has equally spaced ASOC modules. Also, given an identical number of wheels without terrain contact (e.g., 0 no contact and 2 partial contact vs. 1 no contact and 0 partial contact), a robot generally has higher isotropy when terrain contact is lost on the same ASOC, since more modules remain fully engaged with the ground. The isotropy loss from partial contact ASOC modules reinforces the importance of the β axis axle pivot (see Fig. 6).

Finally, a vehicle with a greater number of ASOCs will have a relatively smaller decrease in isotropy for each lost wheel contact, but may have increased difficulty keeping all wheels in contact with the ground due to increased suspension complexity. Introduction of additional modules may also increase mass while decreasing the allowable wheel size and available battery mass given a fixed overall system mass.

2.5 Effect of Terrain Roughness on Isotropy

Isotropy of an omnidirectional robot can also be affected by terrain roughness. Variation in terrain inclination among ASOC modules, or among ASOC module wheel pairs, causes a change in the effective value of L_{split} with respect to the body frame, which yields a change in L_{split} / L_{offset} and thus a change in isotropy (see Fig. 11). Axis β allows ASOC wheels to maintain contact during travel on uneven terrain.

In theory, L_{split} could be modified as a function of terrain inclination via an active, extensible axle to cause the effective L_{split} / L_{offset} ratio to always remain near 2.0, thus yielding good isotropy characteristics on rough terrain. In practice, however, such a design would be cumbersome and impractical. Thus it is useful to examine the effects of terrain inclination on robot isotropy.

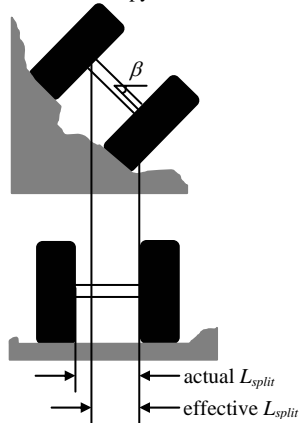


Figure 11. ASOC module on flat and rough terrain. Rough terrain can cause the module to pivot about the β axis, decreasing the effective L_{split} .

In Fig. 12, a contour plot is presented of the average isotropy over a range of static robot configurations and terrain angles. The vehicle in this analysis had equally spaced ASOCs. The results are independent of the number of ASOC modules. The terrain angle was varied for each ASOC independently in a full factorial analysis over each terrain angle

range. It can be seen that the L_{split} / L_{offset} ratio with the largest isotropy value increases with the maximum terrain angle. Larger angles decrease the effective ratio and thus the “true” ratio must increase. Maximum average isotropy also decreases slightly with increasing terrain angle. Table II summarizes these findings.

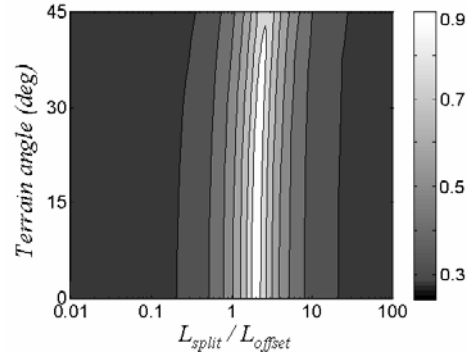


Figure 12. Mean isotropy as a function of L_{split} / L_{offset} and terrain angle.

Table II Effect of Terrain on Isotropy

Terrain angle range	Max isotropy	Optimum
		L_{split} / L_{offset} ratio
0° (flat)	1.000	2.00
0-15°	0.987	2.05
0-30°	0.950	2.27
0-45°	0.895	2.70

3 Design of an Omnidirectional Mobile Robot for Rough Terrain

The class of robots analyzed in this paper is man-portable, battery powered mobile robots with a maximum enclosed envelope of one cubic meter and maximum mass of 65 kg. The primary design objective is to maximize traversable distance over a range of outdoor terrain types while maintaining a high level of mobility. Here, mobility is quantified by the system kinematic isotropy, the ability of an ASOC module to maintain ground contact, and the maximum traversable obstacle height. The robot must operate under its own power, and therefore should maximize mass efficiency to increase its battery payload. It should also minimize power loss from motion resistance in deformable terrain. Factors influencing the design space include wheel width, wheel radius, ASOC split and offset lengths, and the number and relative location of ASOC modules. Geometric constraints that bound the allowable design space must also be considered.

Figure 13 shows an illustration of an omnidirectional mobile robot driven by four ASOC modules. This is a representative configuration that will be considered in this work; however the following analysis is general and applies to robots with N ASOC modules.

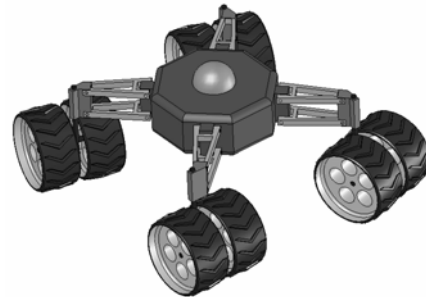


Figure 13. Illustration of an ASOC-driven omnidirectional mobile robot. This robot has four ASOC modules spaced at 90° intervals.

3.1 Geometric Constraints

The unique geometry of the ASOC and the large range of motion of each module constrain the size of some mechanical components. Potentially, a control algorithm could utilize the robot's redundancy to relax these constraints (by ensuring that wheel pairs are never directly oriented towards each other, for example). However, such an algorithm would likely reduce overall system mobility. Therefore, a geometric analysis of the ASOC module workspace is presented here.

3.1.1 ASOC Workspace Analysis

The maximum allowable wheel size that does not risk inter-ASOC interference can be calculated by simple geometric analysis of the module workspace. As seen in Fig. 14, the minimum distance between adjacent ASOC axes, d_a , must be at least twice the maximum radius of the ASOC module workspace, $r_{workspace}$. This radius is the distance from the vertical axis to the most distal point on the wheel:

$$r_{wheel, envelope} = \sqrt{(L_{offset} + r_{wheel})^2 + (0.5L_{split} + t_{wheel})^2}, \quad (3)$$

where L_{offset} and L_{split} are the ASOC split and offset lengths, respectively, and r_{wheel} and t_{wheel} are the wheel radius and width, respectively.

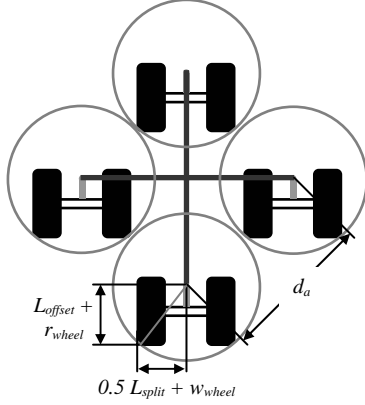


Figure 14. The circles represent the boundaries of the ASOC module workspace. To avoid ASOC interference, they should not intersect.

3.1.2 Maximum Pivot Angle Analysis

In rough terrain, the passive pivot axis (see Fig. 6) allows the ASOC wheels to conform to terrain unevenness. A potential limiting factor of the pivot axis travel is wheel-shaft interference (see Fig. 15).

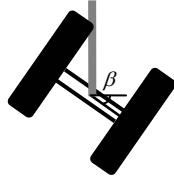


Figure 15. Rear view of ASOC with wheel-shaft interference.

The maximum allowable rotation angle of β can be calculated as the angle at which the inner rim of the wheel intersects the vertical shaft that connects the module to the robot body. This occurs when

$$0.5L_{split} \cos \beta = r_{wheel, effective} \sin \beta \quad (4)$$

where β is the angle of the pivot rotation and $r_{wheel, effective}$ is the vertical distance from the center of the wheel to the section of the rim that intersects the shaft, as shown in Fig. 16.

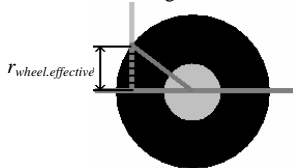


Figure 16. Depiction of $r_{wheel, effective}$.

The value is calculated as

$$r_{wheel, effective} = \sqrt{r_{wheel}^2 - L_{offset}^2}. \quad (5)$$

Note that when $L_{offset} > r_{wheel}$, the shaft and wheel cannot interfere. However, such a configuration could allow obstacles to collide with the ASOC axis before they contact the wheels, which is undesirable. In a nominal configuration, the maximum value of β is given as

$$\beta_{max} = \tan^{-1} \left(\frac{0.5L_{split}}{\sqrt{r_{wheel}^2 - L_{offset}^2}} \right). \quad (6)$$

3.2 Design Optimization

A full factorial design optimization was performed using the objectives discussed in Section 2 (system kinematic isotropy, the ability of an ASOC module to maintain ground contact, and the maximum traversable obstacle height) and constraints outlined in Section 3.1 (workspace limitations, module interference, and maximum suspension travel). The optimization parameters are the number of ASOC modules, L_{split} , L_{offset} , r_{wheel} , and w_{wheel} . An objective function, J , is expressed as a sum of the normalized mobility parameters:

$$J = \frac{K}{K^*} + \frac{\beta_{max}}{\beta_{max}^*} + \frac{h}{h^*} + \frac{d_{max}}{d_{max}^*}, \quad (7)$$

where K is the kinematic isotropy, β_{max} is the maximum β axis pivot angle, h is the maximum traversable obstacle height, and d_{max} is the maximum traversable distance. The star superscript refers to the maximum value of each parameter in the design space. The optimization consisted of a full factorial analysis over the design space to maximize the value of J .

In this analysis, kinematic isotropy and the maximum pivot angle are calculated as described Sections 2.2 and 3.1.2, respectively. The maximum traversable obstacle height is assumed to be a linear function of the wheel radius.

The optimization algorithm estimates maximum traversable distance by first determining the maximum available onboard energy. For the purposes of this study, it is assumed that the vehicle is powered by batteries with an energy density ρ_{energy} of 576 kJ/kg (similar to that of lithium-ion batteries) [18]. The maximum allowable onboard battery mass, $M_{battery}$, is the difference between the non-battery mass (i.e., wheels, structural components, electronics, etc.) and the predetermined total allowable mass. The total allowable mass was chosen as 65 kg. Wheel and ASOC masses are computed as a function of their sizes.

The energy consumed during forward travel is then estimated using an expansion of a semi-empirical formulation for compaction resistance on deformable terrain [19].

$$CR = \frac{n_{wheels}}{(3-n)^{\frac{2n+2}{2n+1}}(n+1)w_{wheel}^{\frac{1}{2n+1}} \left(k_c / w_{wheel} + k_\phi \right)^{\frac{1}{2n+1}}} \left[\frac{3Mg}{\sqrt{r_{wheel}}} \right]^{\frac{2n+2}{2n+1}} \quad (8)$$

In (8), CR is the compaction resistance (N), M is the total vehicle mass (kg), n_{wheels} is the number of wheels (i.e., twice the number of ASOC modules), and n , k_c , and k_ϕ are terrain physical constants (shown in Table III [20, 21]). Note that this estimate holds for straight-line driving and does not consider other resistive forces (such as bulldozing forces) or energy used by other onboard devices.

Table III Terrain Parameters

Terrain type	n	k_c (kPa/m ⁿ⁻¹)	k_ϕ (kPa/m ⁿ)
Dry sand	1.1	0.9	1523.4
Sandy loam	0.7	5.3	1515.0
Clayey soil	0.5	13.2	692.2
Snow	1.6	4.4	196.7

The maximum traversable distance is approximated as

$$d_{\max} = \frac{M_{\text{battery}} \rho_{\text{energy}}}{CR} \quad (9)$$

Since the optimization compares similar systems, motor and drivetrain efficiencies are assumed identical for all candidate designs and therefore are not considered in the calculations.

3.3 Design Optimization Results

Table IV compares the values of the optimized mobility parameters of robots with three, four, and five ASOC modules. The robots were optimized for travel over sandy loam. Results are presented relative to the robot with three ASOC modules.

Table IV Effect of Number of ASOCs on Mobility Parameters

# ASOCs	K	β_{\max}	h	d_{\max}
3	0%	0%	0%	0%
4	0%	0%	0%	-41.4%
5	-2.2%	16.2%	-60.9%	-52.9%

A robot with four ASOC modules has similar values of kinematic isotropy (K), maximum β axis pivot angle (β_{\max}), and maximum traversable obstacle height (h) as a three ASOC robot, however, adding the fourth module decreases available battery mass, and therefore decreases maximum traversable distance (d_{\max}). A fifth ASOC module requires smaller wheels, resulting in lower maximum traversable obstacle height, but higher maximum β axis pivot angle.

Table V shows the values of the optimized geometric parameters for a three ASOC robot. Optimized values were calculated for each of the four terrain types shown in Table III, assuming travel through randomized rough terrain with an angle range of 0-30°. Table VI shows the change in mobility parameter values for optimized designs compared to a baseline design with parameters determined by engineering judgment ($L_{\text{offset}}=0.15$ m, $L_{\text{split}}=0.20$ m, $r_{\text{wheel}}=0.15$ m, $w_{\text{wheel}}=0.03$ m).

Table V Geometric Parameters from Optimization

Terrain type	L_{offset} (m)	L_{split} (m)	r_{wheel} (m)	w_{wheel} (m)
Dry sand	.144	.325	.148	.090
Sandy loam	.144	.325	.148	.112
Clayey soil	.134	.306	.139	.133
Snow	.144	.325	.148	.054

Table VI Mobility Parameter Increases From Optimization

Terrain type	K	β_{\max}	H	d_{\max}
Dry sand	13.2%	85.2%	-1.4%	18.1%
Sandy loam	13.2%	85.2%	-1.4%	29.5%
Clayey soil	12.8%	82.8%	-7.4%	31.9%
Snow	13.2%	85.2%	-1.4%	3.3%

In all cases, the optimized offset lengths were slightly smaller than the wheel radii, which yielded large allowable β tilt angles. The L_{split} to L_{offset} ratios were all near 2.27:1, thus maximizing isotropy for the given terrain roughness range.

As presented, the optimized parameter values for the relatively deformable terrains (i.e. dry sand and snow) resulted in wheels with narrower widths compared to those optimized for relatively rigid terrains (i.e. sandy loam and clayey soil). The thinner widths lead to decreased wheel weight. One could also minimize ground pressure by choosing a wider wheel with smaller radius, but for a given a depth of sinkage, a tall, narrow wheel has significantly less compaction resistance than a short, wide one. For the relatively rigid terrains, a wider wheel was preferred as it allowed a greater onboard battery mass, thus increasing maximum traversable distance.

3.5 Point Vehicle Design

This section presents a point robot design with four ASOC modules (Fig. 17). This robot utilizes a four bar linkage suspension that achieves a maximum travel of 0.33 m. The wheels have a 0.163 m radius, the largest allowed given a body length (L_{body}) of 1 m and the workspace

constraints outlined in Section 3.1.1. A maximum pivot angle of 30° and a high isotropy is achieved with an L_{split} of 0.21 m and an L_{offset} of 0.10 m (see Sections 3.1.2 and 2.5) yielding $L_{\text{split}} / L_{\text{offset}} = 2.1$.

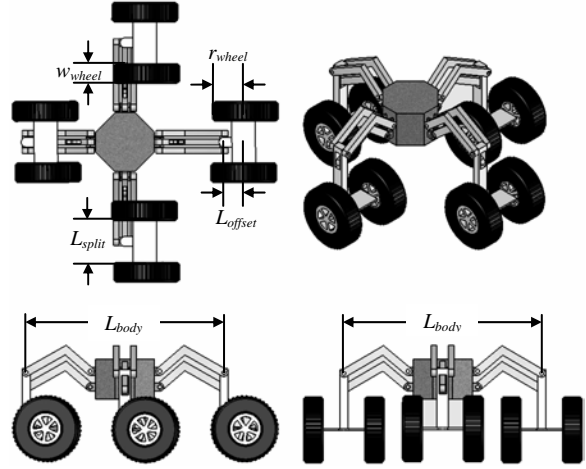


Figure 17. A four view drawing of a point vehicle design.

4 Kinematic Analysis and Control

The previous section presented analysis of an ASOC driven omnidirectional mobile robot for operation in rough terrain. During operation, control systems must coordinate ASOC motion while adapting to terrain unevenness. This section presents a kinematic controller that allows omnidirectional mobility in rough terrain.

4.1 Kinematic Analysis

Coordinate frames for an ASOC driven omnidirectional mobile robot were defined using Devanit-Hartenberg (D-H) notations shown in Table VIII. Coordinate frame assignments are shown in Fig. 18.

Table VIII Joint Representation in D-H Notation

Joint number	d_i	ζ_i	a_i	ξ_i
1_n	0	$2\pi(n-1)/N$	r	0
2_n	h	$-(\alpha+\pi/2)$	0	$\pi/2$
3_n	L_{offset}	$-\beta$	0	0
$4_{n,m}$	0	0	$(-1)^m L_{\text{split}} / 2$	0

In the notation above, d_i is the distance between frame i and frame $i+1$ along the z_{i+1} axis, ζ_i is the angle between x_i and x_{i+1} about z_{i+1} , a_i is the distance from z_i to z_{i+1} along x_{i+1} , ξ_i is the twist angle between z_i and z_{i+1} about x_{i+1} , n is the ASOC number, m is the wheel number, r is the body radius, and h is the vertical distance from the ASOC base to the vehicle body.

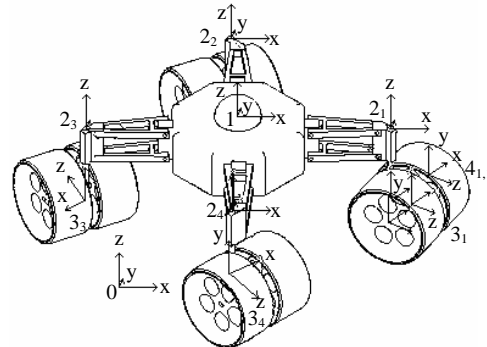


Figure 18. Coordinate frame assignments for an ASOC-driven omnidirectional mobile robot. Note that some wheel and axle frames are hidden for clarity.

Here a three-dimensional model is considered. A body-fixed frame ("1") is allowed 6 DOF with respect to an inertial frame ("0"). The interface of each ASOC module link and the robot body/suspension frame ("2_n") where n refers to the ASOC number and N is the total number of ASOCs) is defined on the body a distance r from the center of the body. A frame ("3_n") at the bottom of each ASOC module link is a distance h below the previous frame and can rotate about axis α . The next frame ("4_n") is defined on the axle at the midpoint between the wheels, and can rotate about β . For convenience, a frame is also defined at the center of each wheel ("5_{n,m}") where n refers to the ASOC number and m refers to the wheel number). These redundant frames are fixed with respect to the axle frame. There is no specified wheel-ground contact frame, as each wheel may have no contact or several moving contact points.

Coordinate transformation matrices are defined as follows:

$$T_1^{2_n} = \begin{bmatrix} \cos(2\pi(n-1)/N) & -\sin(2\pi(n-1)/N) & 0 & r \\ \sin(2\pi(n-1)/N) & \cos(2\pi(n-1)/N) & 0 & 0 \\ 0 & 0 & 1 & 0 \\ 0 & 0 & 0 & 1 \end{bmatrix} \quad (10)$$

$$T_2^{3_n} = \begin{bmatrix} \cos(-(\alpha_n + \pi/2)) & 0 & \sin(-(\alpha_n + \pi/2)) & 0 \\ \sin(-(\alpha_n + \pi/2)) & 0 & -\cos(-(\alpha_n + \pi/2)) & 0 \\ 0 & 1 & 0 & h \\ 0 & 0 & 0 & 1 \end{bmatrix} \quad (11)$$

$$T_3^{4_n} = \begin{bmatrix} \cos(-\beta_n) & -\sin(-\beta_n) & 0 & 0 \\ \sin(-\beta_n) & \cos(-\beta_n) & 0 & 0 \\ 0 & 0 & 1 & L_{offset} \\ 0 & 0 & 0 & 1 \end{bmatrix} \quad (12)$$

$$T_4^{5_{n,m}} = \begin{bmatrix} 1 & 0 & 0 & (-1)^m \frac{L_{split}}{2} \\ 0 & 1 & 0 & 0 \\ 0 & 0 & 1 & 0 \\ 0 & 0 & 0 & 1 \end{bmatrix} \quad (13)$$

where T_p^q is the matrix transforming motion from frame p into frame q . Thus the transformation from the body center frame to the wheel n,m frame is

$$T_1^{5_{n,m}} = T_1^{2_n} T_2^{3_n} T_3^{4_n} T_4^{5_{n,m}} \quad (14)$$

Using these relations, the wheel velocities required to generate a desired body center velocity can be determined.

4.2 Kinematic Control

A simple kinematic control scheme was developed based on the preceding kinematic analysis. Given a desired body translational and rotational velocity defined in an inertial frame, the velocity for each ASOC wheel can be determined despite the effects of terrain unevenness.

First, the velocity of the link between the ASOC module and robot body is computed by:

$$\dot{\mathbf{x}}_{link} = \dot{\mathbf{x}}_{body} + \dot{\phi} r \begin{bmatrix} \cos(\zeta_i) \\ \sin(\zeta_i) \end{bmatrix} \quad (15)$$

where $\dot{\mathbf{x}}_{link}$ and $\dot{\mathbf{x}}_{body}$ are the planar velocity vectors of the link and body, respectively, $\dot{\phi}$ is the yaw rate of the body, and r and ζ_i locate the link i in the body frame. Note that this control method aligns the thrust vectors of each ASOC with the direction of travel, minimizing internal forces. The wheel velocities that yield the desired ASOC link velocity are found as [16]:

$$\dot{\mathbf{x}}_{link} = \begin{bmatrix} \frac{1}{2} \cos(\alpha_n) - \frac{L_{offset}}{L_{split}} \sin(\alpha_n) & \frac{1}{2} \cos(\alpha_n) + \frac{L_{offset}}{L_{split}} \sin(\alpha_n) \\ \frac{1}{2} \sin(\alpha_n) + \frac{L_{offset}}{L_{split}} \cos(\alpha_n) & \frac{1}{2} \sin(\alpha_n) - \frac{L_{offset}}{L_{split}} \cos(\alpha_n) \end{bmatrix} \begin{bmatrix} V_{n,1} \\ V_{n,2} \end{bmatrix} \quad (16)$$

and hence:

$$\begin{bmatrix} V_{n,1} \\ V_{n,2} \end{bmatrix} = \begin{bmatrix} \frac{1}{2} \cos(\alpha_n) - \frac{L_{offset}}{L_{split}} \sin(\alpha_n) & \frac{1}{2} \cos(\alpha_n) + \frac{L_{offset}}{L_{split}} \sin(\alpha_n) \\ \frac{1}{2} \sin(\alpha_n) + \frac{L_{offset}}{L_{split}} \cos(\alpha_n) & \frac{1}{2} \sin(\alpha_n) - \frac{L_{offset}}{L_{split}} \cos(\alpha_n) \end{bmatrix}^{-1} \dot{\mathbf{x}}_{link} \quad (17)$$

where $V_{n,m}$ is the forward linear velocity of wheel n,m in the wheel frame ("5_{n,m}"), and is computed as $V_{n,m} = R\omega_{n,m}$ where R is the wheel radius and $\omega_{n,m}$ is the wheel angular speed. Angular velocity is controllable via simple PD or other schemes.

Terrain roughness causes ASOC modules to tilt (i.e. rotate about β). Wheel velocities then possess non-zero components in the body's z dimension. The effects of module tilt can be compensated in the controller via computation of an effective L_{split} (see Fig. 11). The wheel velocity component in the body's x - y plane appears on the left side of (18). Inclusion of the effects of out of plane wheel velocity components in (17) yields:

$$\begin{bmatrix} V_{n,1} \cos \gamma_{n,1} \\ V_{n,2} \cos \gamma_{n,2} \end{bmatrix} = \begin{bmatrix} \frac{\cos(\alpha_i)}{2} - \frac{L_{offset}}{L_{split} \cos(\beta_i)} \sin(\alpha_i) & \frac{\cos(\alpha_i)}{2} + \frac{L_{offset}}{L_{split} \cos(\beta_i)} \sin(\alpha_i) \\ \frac{\sin(\alpha_i)}{2} + \frac{L_{offset}}{L_{split} \cos(\beta_i)} \cos(\alpha_i) & \frac{\sin(\alpha_i)}{2} - \frac{L_{offset}}{L_{split} \cos(\beta_i)} \cos(\alpha_i) \end{bmatrix}^{-1} \dot{\mathbf{x}}_{link} \quad (18)$$

where $\gamma_{n,m}$ is the angle between the velocity vector of wheel n,m and the x - y plane in the body-fixed frame (see Fig. 19).

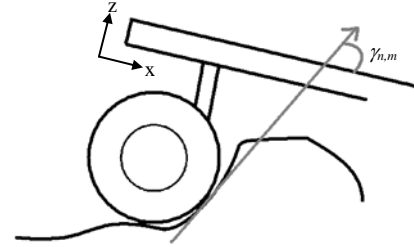


Figure 19. Wheel-terrain contact angle, $\gamma_{n,m}$. The gray vector is parallel to the velocity of the wheel.

Figure 20 shows a block diagram of a scheme for rough terrain omnidirectional mobile robot control. The input is a desired velocity profile defined in the inertial frame. It is assumed that the robot's full state can be estimated. The desired velocity profile is converted to a desired velocity in the body-fixed frame based on the robot's current position and orientation. ASOC module link velocities are then computed via (15). Desired wheel velocities can then be calculated using (18), here assuming knowledge or estimates of wheel-terrain contact angles. Wheel-terrain contact angles can be estimated via axle-mounted force sensors (to measure wheel-terrain interaction normal force direction) or via kinematic estimators [21]. PD controllers command each wheel to track the desired wheel velocities. Actual velocities can be determined via odometry; however more sophisticated methods (such as visual odometry) are required to estimate wheel slip [22].

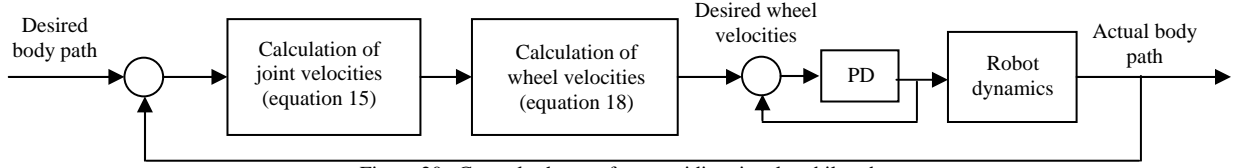


Figure 20. Control scheme of an omnidirectional mobile robot.

4.3 Simulation Results

A dynamic model of an ASOC-driven mobile robot was developed to study the performance of the control method described above. The kinematic controller was implemented to allow the robot to track a desired velocity profile over rough terrain. Independent PD control loops allowed each wheel to track its desired velocity.

The robot parameters for the simulation were as follows: body length=1 m, total mass=65 kg, wheel radius=0.10 m, $L_{split}=0.20$ m, $L_{offset}=0.10$ m. The control gains for each wheel were $K_p=7.3$, $K_d=0.02$. Wheel-terrain interaction forces were determined via a simple coulomb friction model with $\mu=0.6$. Terrain elevation was modeled as a triangularized mesh with elevation points possessing a standard deviation of σ . In initial simulations it was assumed that the robot possessed perfect knowledge of wheel-terrain contact angles. Wheel-terrain contact locations were determined by making a thin wheel approximation and finding the intersection points between the wheel and the local triangular mesh patches.

To study the omnidirectional capability of the robot, a desired 4.5 m square path was commanded at a constant speed of 1.5 m/s. This corresponds to 1.5 body lengths/second.

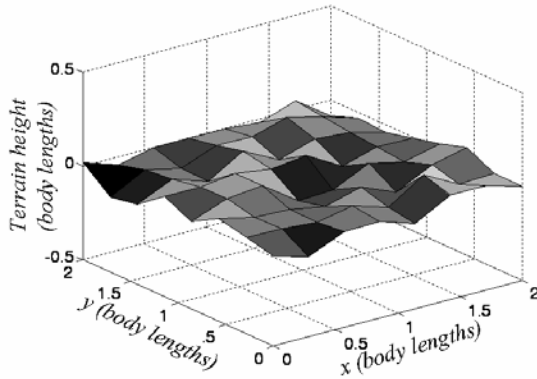


Figure 21. Example of terrain used in simulation, with $\sigma = 4.5$.

In the following simulations, σ was chosen as 0, 1.5, 3.0, and 4.5 cm, yielding maximum terrain inclination angles of approximately 0° , 20° , 35° , and 45° , respectively.

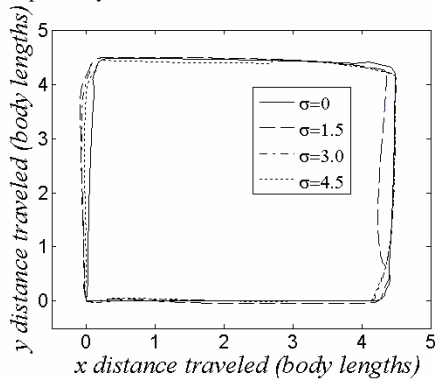


Figure 22. Top view of robot path tracking a square on rough terrain.

In Fig. 22 it can be seen that the robot was able to track the desired path with good fidelity, even in very rough terrain. In these simulations, the controller had error and noise-free, continuous absolute position data. Table IX presents the RMS error for this trial for each terrain roughness.

Table IX RMS path tracking error for several terrain heights

σ	RMS error (% body)
0.0	8.67
1.5	8.89
3.0	10.48
4.5	11.59

Although an omnidirectional robot can kinematically perform zero radius turns at any velocity, dynamic effects may reduce path tracking capability at higher velocities. Figure 23 shows that the vehicle is able to maintain a high velocity magnitude when the body was changing direction. During these simulations, the velocity never dropped below 48% of the nominal commanded velocity.

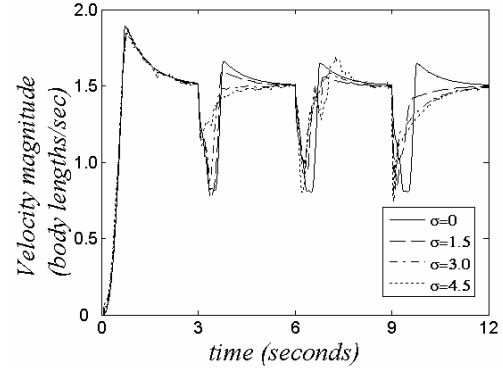


Figure 23. Velocity magnitude during path tracking.

Further simulations were conducted to study the effects of utilizing wheel-terrain contact angle knowledge in the controller and knowledge of robot absolute position. Simulations were run with and without absolute position updates at 0.5 Hz and with and without knowledge of wheel-terrain contact angle. Simple dead reckoning was used estimate vehicle position in simulations without absolute position knowledge and to interpolate between updates in simulations with absolute position knowledge. Path tracking results are shown in Fig. 24. Numerical results are shown in Table X.

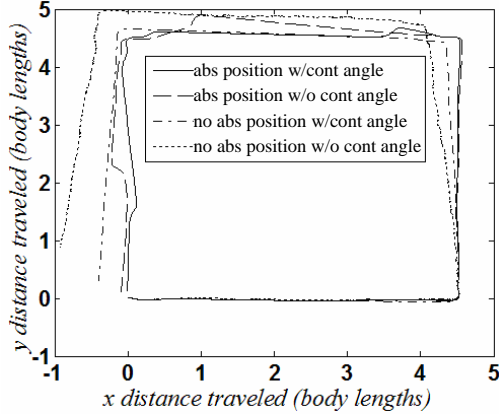


Figure 24. Top view of the body trace during square tracking on rough terrain for varying levels of controller knowledge.

Table X RMS path tracking error for varying controller knowledge

Controller Knowledge	RMS error (% body)
Absolute position w/ contact angle	6.96
Absolute position w/o contact angle	17.71
No absolute position w/ contact angle	21.28
No absolute position w/o contact angle	86.31

Note that the path tracking error in simulations with absolute position information is bounded, while the tracking error in simulations without absolute position data is not. When absolute position information is not available, a 75.3% reduction in path tracking error is seen when the vehicle controller uses wheel-terrain contact angle information. This is useful for the many situations where position information from GPS, for example, may be unavailable. Even with absolute position updates, path tracking error is reduced by 60.7% when the controller wheel-terrain contact angle information.

5 Conclusions

In this paper, the design and control of an omnidirectional mobile robot driven by active split offset casters for use in rough terrain has been studied. An isotropy analysis was conducted to determine the optimal geometry and layout of the ASOC modules. This analysis indicates that equally spaced modules with $L_{split} / L_{offset} = 2.0$ yield a robot with equal mobility capability in all directions on flat terrain. On rough terrain, a larger ratio is desired, and robot isotropy degrades slightly. It also shows that isotropy is independent of wheel radius, which increases the scalability of the design.

Numerous design considerations for omnidirectional mobile robots were presented. An optimization algorithm was implemented to derive values for ASOC module and wheel geometries. For illustration, a man portable robot was designed, but the geometric constraints and the optimization algorithm are scalable and can be applied to robots of any size. It was shown that the designs suggested by the optimization have improved performance when compared to a non-optimized design. Through deliberate ASOC geometric parameter selection, it was possible to increase estimated traverse distance and mobility versus a baseline design.

A kinematic controller was developed and its performance was studied on both flat and rough terrain. The effects of wheel-terrain contact angle information and absolute position knowledge on performance were studied. Simulation results showed that an omnidirectional mobile robot is able to track a square trajectory with good performance despite local terrain inclinations angles near 45° . It was also shown that substantial path tracking improvements were possible if wheel-terrain contact angle information was used in the controller.

6 References

- [1] Fish, S., "UGV's in Future Combat Systems," *Proceedings of SPIE - The International Society for Optical Engineering*, v 5422, *Unmanned Ground Vehicle Technology VI*, pp. 288-291, Apr 2004.
- [2] Blich, J., "Artificial Intelligence Technologies for Robot Assisted Urban Search and Rescue," *Expert Systems with Apps*, 1996.
- [3] Erickson, J., "Living the Dream: An Overview of the Mars Exploration Project," *IEEE Robotics and Automation*, v 13, n 2, pp. 12-18, Jun 2006.
- [4] Cheng, J., Gao, L., Wang, H., "Steering Analysis of Tracked Vehicles Based on Skid Condition," *Chinese Journal of Mechanical Engineering*, v 42, pp. 192-195, May 2006.
- [5] Ishigami, G., Miwa, A., Yoshida, K., "Steering Trajectory Analysis of Planetary Exploration Rovers Based on All-Wheel Dynamics Model," *Proc of the 8th Intl Symposium on Artificial Intelligence, Robotics and Automation in Space*, pp. 121-128, 2005.
- [6] Iagnemma, K. and Dubowsky, S., *Mobile Robots in Rough Terrain: Estimation, Motion Planning, and Control with Application to Planetary Rovers*, Springer Tracts in Advanced Robotics (STAR) Series, Vol. 12, Springer, 2004.
- [7] Fujisawa, S., Ohkubo, K., Yoshida, T., Satonaka, N., Shidama, Y., and Yamaura, H., "Improved Moving Properties of an Omnidirectional Vehicle Using Stepping Motor," *Proc of the 36th Conf on Decision & Control*, San Diego, pp.3654-3657, 1997.
- [8] Williams, R., Carter, B., Gallina, P., and Rosati, G., "Wheeled Omni-directional Robot Dynamics Including Slip," *Proc of 2002 ASME Design Engineering Technical Conferences*, Sep 2002.
- [9] Muir, P., and Neuman, C., "Kinematic Modeling for Feedback Control of an Omnidirectional Wheeled Mobile Robot," *Proc. of 1987 IEEE Intl Conf on Robotics and Automation*, 1987.
- [10] Bradley A., Miller, S., Creary, G., Miller, N., Begley, M., Misch, N., "Mobius, an Omnidirectional Robot Utilizing Mecanum Wheels and Fuzzy Logic Control," *Proc of the 28th Annual AAS Rocky Mountain Guidance and Control Conf*, pp. 251-266, 2005.
- [11] Ferriere L., Raucant B., "ROLLMOBS, a New Universal Wheel Concept," *Proceedings of 1998 IEEE Intl Conf on Robotics and Automation*, pp. 1877-1882, Leuven, , May 1998.
- [12] West, A.M., and Asada, H., "Design of Ball Wheel Mechanisms for Omnidirectional Vehicles with Full Mobility and Invariant Kinematics," *ASME Journal of Mechanical Design*, 117, 1995.
- [13] Carlson, J., Murphy, R., "How UGVs Physically Fail in the Field," *IEEE Transactions on Robotics*, v 21, n 3, Jun 2005.
- [14] Wood, C., Davidson, M., Rich, S., Keller, J., and Maxfield, R., "T2 Omni-Directional Vehicle Mechanical Design," *Proceedings of the SPIE Conference on Mobile Robots XIV*, Boston, pp. 69-76, Sep 1999.
- [15] Park, T., Lee, J., Yi, B., Kim, W., You, B., Oh., "Optimal Design and Actuator Sizing of Redundantly Actuated Omnidirectional Mobile Robots," *IEEE Intl Conf on Robotics and Automation*, pp.732-7, 2002.
- [16] Yu, H., Dubowsky, S., and Skwersky, A., "Omni-directional Mobility Using Active Split Offset Castors," *Proc of the 26th Biennial Mechanisms and Robotics Conf of the 2000 ASME Design Engineering Technical Conferences*, Sep 2000.
- [17] Spenko, M., Yu, H., and Dubowsky, S., "Analysis and Design of an Omnidirectional Platform for Operation on Non-Ideal Floors," *Proc of the 2002 IEEE Intl Conf on Robotics and Automation*, Washington, DC, May 2002.
- [18] Minami, T., Tatsumisago, and M., Wakihara, M. *Solid state ionics for batteries*. Berlin: Springer, 2004.
- [19] Bekker G. *Theory of land locomotion, the mechanics of vehicle mobility*. Ann Arbor: The University of Michigan Press; 1956.
- [20] Yong R, Fattah E, Skiadas N. *Vehicle traction mechanics*. Amsterdam: Elsevier Science Publishers; 1984.
- [21] Wong J. *Terramechanics and offroad vehicles*. Amsterdam: Elsevier Science Publishers; 1989.
- [22] Cheng, Y., Maimone, M., and Matthies, L., "Visual Odometry on the Mars Exploration Rovers," *IEEE Robotics and Automation*, v 13, n 2, pp. 54-62, Jun 2006.